The Astrophysical Journal Letters, 961:L41 (25pp), 2024 February 1 https://doi.org/10.3847/2041-8213/ad19c4

Spectacular Nucleosynthesis from Early Massive Stars

Alexander P. Ji[1,2,3], Sanjana Curtis[1,4,41], Nicholas Storm[5], Vedant Chandra[6], Kevin C. Schlaufman[7,8], Keivan G. Stassun[9], Alexander Heger[3,10,11], Marco Pignatari[12,13,14], Adrian M. Price-Whelan[15], Maria Bergemann[5], Guy S. Stringfellow[16], Carla Fröhlich[3,17], Henrique Reggiani[18,42], Erika M. Holmbeck[18,43], Jamie Tayar[19], Shivani P. Shah[19], Emily J. Griffith[16,41], Chervin F. P. Laporte[20,21], Andrew R. Casey[22,23], Keith Hawkins[24], Danny Horta[15], William Cerny[25], Pierre Thibodeaux[1], Sam A. Usman[1], João A. S. Amarante[26,27], Rachael L. Beaton[28], Phillip A. Cargile[6], Cristina Chiappini[29], Charlie Conroy[6], Jennifer A. Johnson[30,31], Juna A. Kollmeier[18,32], Haining Li[33], Sarah Loebman[34], Georges Meynet[35], Dmitry Bizyaev[36,37], Joel R. Brownstein[38], Pramod Gupta[39], Sean Morrison[40], Kaike Pan[36], Solange V. Ramirez[18], Hans-Walter Rix[5], and José Sánchez-Gallego[39]

[1] Department of Astronomy & Astrophysics, University of Chicago, 5640 South Ellis Avenue, Chicago, IL 60637, USA; alexji@uchicago.edu
[2] Kavli Institute for Cosmological Physics, University of Chicago, Chicago, IL 60637, USA
[3] Joint Institute for Nuclear Astrophysics—Center for Evolution of the Elements (JINA), East Lansing, MI 48824, USA
[4] Department of Astronomy, University of California, Berkeley, Berkeley, CA 94720, USA
[5] Max Planck Institute for Astronomy, Königstuhl 17, D-69117 Heidelberg, Germany
[6] Center for Astrophysics | Harvard & Smithsonian, 60 Garden Street, Cambridge, MA 02138, USA
[7] Johns Hopkins University William H. Miller III Department of Physics & Astronomy, 3400 North Charles Street, Baltimore, MD 21218, USA
[8] Tuve Fellow, Carnegie Institution for Science Earth & Planets Laboratory, 5241 Broad Branch Road NW, Washington, DC 20015, USA
[9] Department of Physics and Astronomy, Vanderbilt University, Nashville, TN 37235, USA
[10] School of Physics and Astronomy, Monash University, Melbourne, VIC 3800, Australia
[11] Center of Excellence for Astrophysics in Three Dimensions (ASTRO-3D), Stromlo, ACT 2611, Australia
[12] Konkoly Observatory, Research Centre for Astronomy and Earth Sciences, Eötvös Loránd Research Network (ELKH), Konkoly Thege Miklós út 15-17, H-1121 Budapest, Hungary
[13] CSFK, MTA Centre of Excellence, Budapest, Konkoly Thege Miklós út 15-17, H-1121, Hungary
[14] E. A. Milne Centre for Astrophysics, University of Hull, Hull HU6 7RX, UK
[15] Center for Computational Astrophysics, Flatiron Institute, 162 Fifth Avenue, New York, NY 10010, USA
[16] Center for Astrophysics and Space Astronomy, University of Colorado, 389 UCB, Boulder, CO 80309-0389, USA
[17] Department of Physics, North Carolina State University, Raleigh, NC 27695, USA
[18] The Observatories of the Carnegie Institution for Science, 813 Santa Barbara Street, Pasadena, CA 91101, USA
[19] Department of Astronomy, University of Florida, Bryant Space Science Center, Stadium Road, Gainesville, FL 32611, USA
[20] Institut de Ciències del Cosmos (ICCUB), Universitat de Barcelona, Martí i Franquès 1, E-08028 Barcelona, Spain
[21] Institut d'Estudis Espacials de Catalunya (IEEC), E-08034 Barcelona, Spain
[22] School of Physics & Astronomy, Monash University, Wellington Road, Clayton, VIC 3800, Australia
[23] ARC Centre of Excellence for All Sky Astrophysics in 3 Dimensions (ASTRO 3D), Canberra, ACT 2611, Australia
[24] Department of Astronomy, The University of Texas at Austin, 2515 Speedway Boulevard, Austin, TX 78712, USA
[25] Department of Astronomy, Yale University, New Haven, CT 06520, USA
[26] Institut de Ciencies del Cosmos (ICCUB), Universitat de Barcelona (IEEC-UB), Martí i Franquès 1, E-08028 Barcelona, Spain
[27] Jeremiah Horrocks Institute, University of Central Lancashire, Preston, PR1 2HE, UK
[28] Space Telescope Science Institute, 3700 San Martin Drive, Baltimore, MD 21218, USA
[29] Leibniz-Institut für Astrophysik Potsdam (AIP), An der Sternwarte 16, D-14482 Potsdam, Germany
[30] Department of Astronomy, The Ohio State University, 140 West 18th Avenue, Columbus, OH 43210, USA
[31] Center for Cosmology and AstroParticle Physics, Ohio State University, 191 West Woodruff Avenue, Columbus, OH 43210, USA
[32] Canadian Institute for Theoretical Astrophysics, University of Toronto, Toronto, ON, M5S-98H, Canada
[33] Key Lab of Optical Astronomy, National Astronomical Observatories, Chinese Academy of Sciences, A20 Datun Road, Chaoyang, Beijing 100012, People's Republic of China
[34] Department of Physics, University of California, Merced, 5200 North Lake Road, Merced, CA 95343, USA
[35] Department of Astronomy of Geneva University, Switzerland
[36] Apache Point Observatory and New Mexico State University, P.O. Box 59, Sunspot, NM 88349-0059, USA
[37] Sternberg Astronomical Institute, Moscow State University, Moscow
[38] Department of Physics and Astronomy, University of Utah, 115 S. 1400 E., Salt Lake City, UT 84112, USA
[39] Department of Astronomy, University of Washington, Box 351580, Seattle, WA 98195, USA
[40] Department of Astronomy, University of Illinois at Urbana-Champaign, Urbana, IL 61801, USA
Received 2023 October 20; revised 2023 December 23; accepted 2023 December 30; published 2024 January 31

Abstract

Stars that formed with an initial mass of over 50 $M_{\odot}$ are very rare today, but they are thought to be more common in the early Universe. The fates of those early, metal-poor, massive stars are highly uncertain. Most are expected to

[41] NSF Astronomy and Astrophysics Postdoctoral Fellow.
[42] Carnegie Fellow.
[43] NHFP Hubble Fellow.

directly collapse to black holes, while some may explode as a result of rotationally powered engines or the pair-creation instability. We present the chemical abundances of J0931+0038, a nearby low-mass star identified in early follow-up of the SDSS-V Milky Way Mapper, which preserves the signature of unusual nucleosynthesis from a massive star in the early Universe. J0931+0038 has a relatively high metallicity ([Fe/H] $= -1.76 \pm 0.13$) but an extreme odd–even abundance pattern, with some of the lowest known abundance ratios of [N/Fe], [Na/Fe], [K/Fe], [Sc/Fe], and [Ba/Fe]. The implication is that a majority of its metals originated in a single extremely metal-poor nucleosynthetic source. An extensive search through nucleosynthesis predictions finds a clear preference for progenitors with initial mass $>50\ M_\odot$, making J0931+0038 one of the first observational constraints on nucleosynthesis in this mass range. However, the full abundance pattern is not matched by any models in the literature. J0931+0038 thus presents a challenge for the next generation of nucleosynthesis models and motivates the study of high-mass progenitor stars impacted by convection, rotation, jets, and/or binary companions. Though rare, more examples of unusual early nucleosynthesis in metal-poor stars should be found in upcoming large spectroscopic surveys.

Unified Astronomy Thesaurus concepts: Core-collapse supernovae (304); Nucleosynthesis (1131); Nuclear astrophysics (1129); Population II stars (1284); Population III stars (1285); Galactic archaeology (2178); Stellar abundances (1577); Hypernovae (775); Chemically peculiar stars (226)

1. Introduction

The chemical abundances of metal-poor stars provide an archaeological snapshot of the first massive stars (e.g., Frebel & Norris 2015). When those stars died, they ejected elements that polluted the interstellar and intergalactic medium. Stars forming out of this minimally polluted gas would be metal-poor, and the low-mass metal-poor stars could survive until today, where they can be found in our Milky Way. The atmospheres of these low-mass stars thus provide a window to nucleosynthesis in the first massive stars. Since even JWST is unable to directly observe the first massive stars (e.g., Schauer et al. 2020), these chemical abundances are one of the few ways to understand how the first stars formed and died. Theoretically, one of the most robust predictions is that the first metal-free stars should have a top-heavy initial mass function with a characteristic mass of $\gtrsim 10\ M_\odot$ (e.g., Bromm 2013; Klessen & Glover 2023). This prediction, however, is still not confirmed observationally, nor is there a clear understanding of when or how the initial mass function transitions to its present-day shape (e.g., Offner et al. 2014; Sharda & Krumholz 2022).

Decades of searches have led to the discovery and chemical characterization of hundreds of extremely metal-poor stars with [Fe/H] $\lesssim -3$ (e.g., Beers et al. 1992; Cayrel et al. 2004; Frebel et al. 2006; Schlaufman & Casey 2014; Aguado et al. 2016; Starkenburg et al. 2017; Li et al. 2018; Da Costa et al. 2019). Their chemical compositions reveal a variety of processes occurring in the early Universe. The majority of these metal-poor stars broadly look like they have been enriched by core-collapse supernovae (CCSNe), possibly following a standard Salpeter initial mass function (e.g., Cayrel et al. 2004; Heger & Woosley 2010). A prominent signature is the carbon-enhanced metal-poor stars, which make up the majority of stars at [Fe/H] $\lesssim -4$ (e.g., Norris et al. 2013; Placco et al. 2014) and may suggest that the first stars preferentially explode as faint supernovae (e.g., Umeda & Nomoto 2002) or have extremely rapid rotation and winds (e.g., Meynet et al. 2006; Chiappini 2013). A few iron-poor stars have been found without carbon enhancement, making them stars with the lowest overall metallicities (e.g., Caffau et al. 2013; Starkenburg et al. 2017). There also have been many signatures of high-energy hypernovae (HNe), accompanied by a variety of neutron-capture nucleosynthesis signatures (e.g., Ezzeddine et al. 2019; Skúladóttir et al. 2021; Yong et al. 2021). Recently, the first signature of pair-instability supernovae (PISNe) was finally found (Xing et al. 2023; though a CCSN interpretation has also been suggested by Jeena et al. 2023).

Interestingly, when comparing the abundances of metal-poor stars to nucleosynthesis models, almost all the supernova progenitors have initial masses less than $50\ M_\odot$ (e.g., Placco et al. 2015; Fraser et al. 2017; Ishigaki et al. 2018). This could be because more massive stars typically collapse to black holes, either directly or after pair-instability pulsation-driven mass loss, and thus do not release any metals into the Universe (e.g., Heger et al. 2003; Yoon et al. 2012).

The community's attention has primarily been focused on extremely metal-poor stars with [Fe/H] $\lesssim -3$. Such metal-poor stars are likely enriched by only a few supernovae, or even just one supernova (Audouze & Silk 1995; Ryan et al. 1996), so it is reasonable to compare their chemical abundances to nucleosynthesis models of individual supernova explosions. However, in principle, it is possible to find stars dominated by nucleosynthesis in a small number of supernovae at higher metallicities. For example, it is well known that PISNe produce so much calcium and iron that they immediately enrich stars to [Fe/H] ~ -2, which would make them difficult to discover in surveys looking for the most Fe-poor stars (Karlsson et al. 2008; Salvadori et al. 2019). Identifying such relatively metal-rich stars with unique elemental compositions is difficult, because the vast majority of stars at [Fe/H] > -3 have experienced ordinary chemical evolution, so it is hard to distinguish interesting stars from a vast background of ordinary stars. Stars at higher metallicities could be hiding signatures of a different population of supernovae that produce large amounts of iron.

Here, we present the discovery and chemical composition of the spectacular star 2MASS J09311004+0038042 (Gaia DR3 3841101888330639872, abbreviated as J0931+0038), which was identified in early Sloan Digital Sky Survey V (SDSS-V) data. J0931+0038 has a relatively high metallicity [Fe/H] $= -1.76$, but its extremely low abundances of other elements like Na, K, Sc, and Ba show that it is dominated by nucleosynthesis from a single source. The star's composition is unlike any star that has been seen before, and its high metallicity and abundance pattern imply a progenitor star with an initial mass of over $50\ M_\odot$, one of the first and most complete observational constraints on nucleosynthesis in this mass range. However, we have been unable to find satisfactory nucleosynthesis models to explain the full abundance

pattern. Section 2 describes our target selection, observations, and chemical abundance analysis. Section 3 compares the results of the abundance analysis to existing stellar abundances. We discuss the origin of this star in Section 4 and conclude in Section 5. An extended Appendix provides details on the abundance analysis (Appendix A) and nucleosynthesis fits (Appendix B).

2. Observations and Analysis

2.1. Target Selection and Observations

J0931+0038 was observed by SDSS-V (Kollmeier et al. 2017; Almeida et al. 2023; N. De Lee et al. 2024, in preparation) in the metal-poor halo program, which uses spare fibers to target stars with photometric metallicities [Fe/H]< -2. This particular star was identified as a metal-poor candidate with SkyMapper DR2 photometry (Onken et al. 2019) and observed with the low-resolution optical BOSS spectrograph. The BOSS spectra were analyzed using `MINESweeper` (Cargile et al. 2020), which performs a spectrophotometric fit including the Gaia DR3 parallax, broadband photometry, and the MIST isochrones (Choi et al. 2016). The `MINESweeper` parameters were $T_{\rm eff} = 5220$ K, $\log g = 2.57$, $[{\rm Fe/H}] = -1.9$, and $[\alpha/{\rm Fe}] = 0.03$, showing it to be a metal-poor and alpha-poor red giant. The star has an eccentric halo orbit and is likely unassociated with any known structures (see Appendix A).

We observed J0931+0038 with Magellan/MIKE (Bernstein et al. 2003) for 3 hr on 2023 April 13, obtaining a high signal-to-noise ratio $R \sim 30{,}000$ spectrum (100 per pixel or 70 per resolution element at 4000 Å). The data were reduced with CarPy (Kelson 2003). Portions of this spectrum are shown in Figure 1 compared to two stars of similar stellar parameters and metallicities: a Keck/HIRES spectrum of the *r*-process-enhanced star BD +17°3248 (Cowan et al. 2002; Johnson & Bolte 2002) and a Magellan/MIKE spectrum of Gaia DR3 3963318275114883584, a star with ordinary composition. Just visually, the spectrum of J0931+0038 displays extraordinarily weak Na, Ti, Sc, and Ba lines; unusually strong lines of Sr, Y, Mn, Ni, and Zn; and clear detections of Mo, Ru, and Pd.

2.2. Abundance Analysis

We performed a standard analysis using 1D ATLAS model atmospheres (Castelli & Kurucz 2003) and the MOOG radiative transfer code including scattering (Sneden 1973; Sobeck et al. 2011) and assuming local thermodynamic equilibrium (LTE).[44] The line list was selected from a combination of lines from Roederer et al. (2018) and Ji et al. (2020a), with atomic data adopted from `linemake`[45] (Placco et al. 2021). Stellar parameters were derived by fixing spectrophotometric temperatures and then determining other stellar parameters spectroscopically, resulting in $T_{\rm eff} = 5200 \pm 100$ K, $\log g = 2.75 \pm 0.20$, $\nu_t = 1.65 \pm 0.3\,{\rm km\,s^{-1}}$, $[{\rm M/H}] = -1.9 \pm 0.1$, and $[\alpha/{\rm Fe}] = 0.0$. Chemical abundances were determined using `smhr` (Casey 2014)[46] with a mix of equivalent widths and syntheses. Upper limits were calculated using synthetic spectra. The adopted abundance uncertainty includes line-to-line scatter, signal-to-noise ratio, and stellar parameter uncertainties. [Fe/H] uncertainties are on the total metallicity, while [X/Fe] uncertainties are relative to [Fe/H]. Non-LTE (NLTE) corrections were mostly calculated using `TSFitPy`[47] (Gerber et al. 2023). The actual [Fe/H] abundance after NLTE corrections is $[{\rm Fe/H}] = -1.76 \pm 0.13$. We also estimated evolutionary corrections for C and N based on metal-poor giants in APOGEE DR17 (Abdurro'uf et al. 2022). Full details of the analysis are given in Appendix A.

3. Abundance Results

Table 1 presents the chemical abundances of J0931+0038, in NLTE where available. Figure 2 shows [X/Fe] compared to the SAGA database after removing upper limits (Suda et al. 2008). We adopt the Solar abundance scale from Magg et al. (2022a), using Asplund et al. (2009) to fill in missing elements. The SAGA database abundances are shifted to this abundance scale. The SAGA database predominantly consists of LTE abundances, so for comparison, we also shift the SAGA abundances by the NLTE corrections for J0931+0038 in Table 1.

There are four remarkable features in the abundance pattern of J0931+0038. First, the light elements from C to Sc display an extremely strong odd–even effect, comparable only to the recently discovered "pair-instability" star J1010+2358 (Xing et al. 2023). Second, the abundances of the light iron-peak elements Sc, Ti, and V are extremely low, similar to some metal-poor stars in the bulge, halo, and dwarf galaxies (Casey & Schlaufman 2015; Ji et al. 2020b). Third, the heavier iron-peak elements Mn, Ni, and Zn are quite enhanced, which matches some extremely metal-poor stars associated with HNe (Ezzeddine et al. 2019; Skúladóttir et al. 2021; Yong et al. 2021). Fourth, the neutron-capture elements around the first peak (magic neutron number $N = 50$) from Sr to Pd are highly enhanced, similar to stars like HD 122563 and HD 88609 (Honda et al. 2007), but the [Ba/Fe] is one of the lowest values ever measured, comparable to the most extreme stars in ultra-faint dwarf galaxies (Ji et al. 2019). While each of these four features has been seen before in individual stars, J0931+0038 displays one of the most extreme versions of each feature and combines all of them in one star. Additionally, all previously known stars with such extreme abundance features have been found in the very metal-poor regime at $[{\rm Fe/H}] \lesssim -2.5$, but J0931+0038 has a metallicity over 5× higher, $[{\rm Fe/H}] = -1.76$.

4. Discussion

4.1. A Single Enrichment Source

J0931+0038 has a relatively high metallicity and would normally be considered heavily contaminated by chemical evolution, but the very low abundances of N, Na, K, Sc, and Ba imply that it has negligible contamination from general chemical evolution in the interstellar medium (ISM). Figure 3 illustrates this by plotting the [X/H] versus [Fe/H] of J0931+0038 and the SAGA database, including dwarf galaxy stars from JINAbase (Abohalima & Frebel 2018; other elements shown in Appendix A). It is clear that J0931+0038 is not part of any overall chemical evolution trend, either in Milky Way halo stars or in all known dwarf galaxies.

A newly formed star's metallicity is the sum of the metallicities of the background ISM and the diluted ejecta from any recent nucleosynthetic sources. Thus, one way to interpret Figure 3 is that 100% of the Na and Ba in J0931+0038 comes

[44] https://github.com/alexji/moog17scat
[45] https://github.com/vmplacco/linemake
[46] https://github.com/andycasey/smhr
[47] https://github.com/TSFitPy-developers/TSFitPy

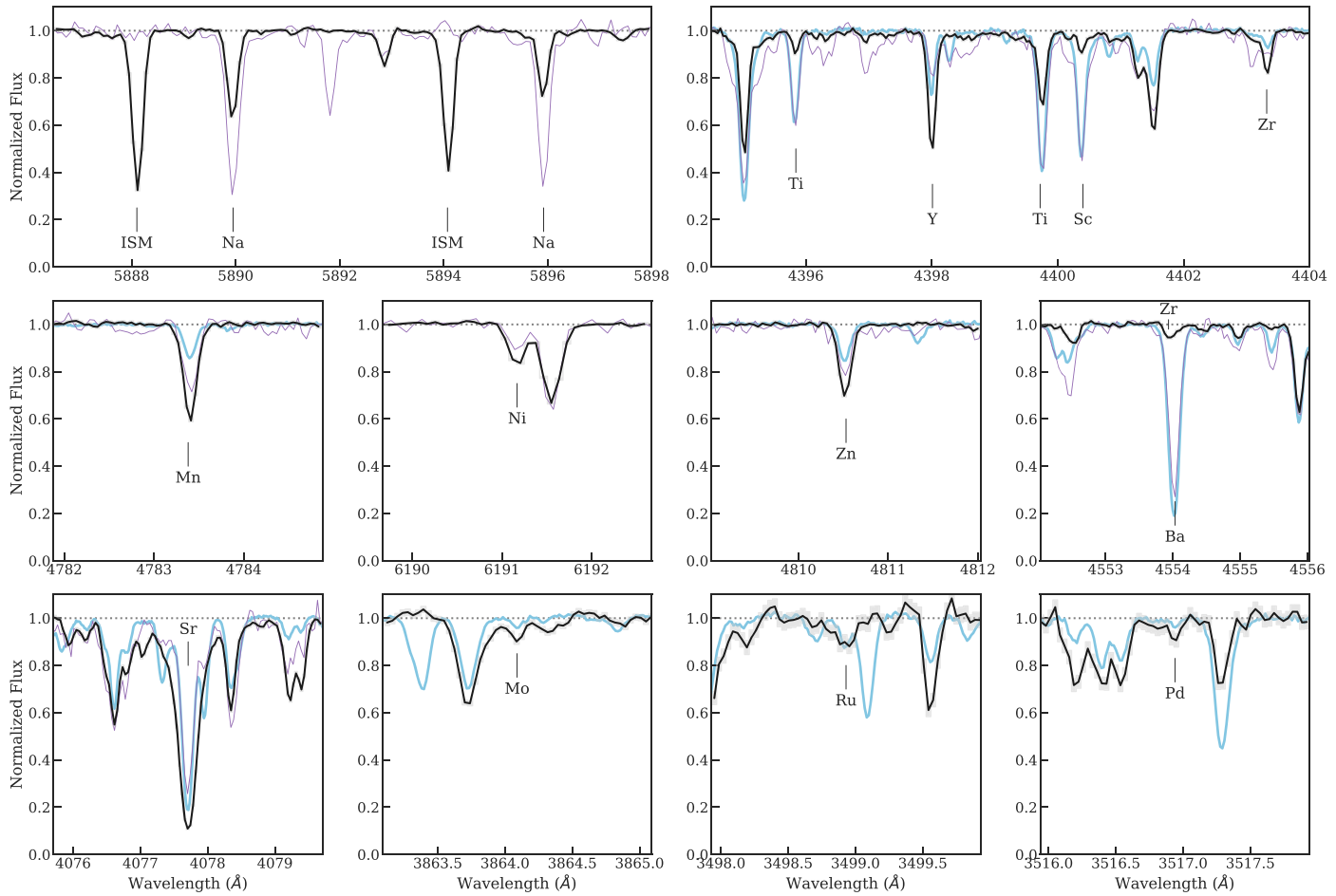

Figure 1. Spectrum of J0931+0038 (black line and gray shaded uncertainty band). For comparison, two stars with similar stellar parameters are plotted: a MIKE spectrum of a normal star from our SDSS sample in purple and a Keck/HIRES spectrum of the *r*-process-enhanced star BD +17°3248 in blue. Visible by eye are the low abundances of Na, Ti, Sc, and Ba; the enhancement in Sr, Y, Mn, Ni, and Zn; and the detected Mo, Ru, and Pd lines. BD +17°3248 is highly *r*-process-enhanced, but J0931+0038 has stronger lines of Sr, Mo, Ru, and Pd, while the Ba line is barely detected (it is blended with a weak Zr line).

from swept-up ISM material. This would imply that it formed from ISM composition of $[Fe/H] \sim -3.5$ (red dashed lines in Figure 3). A recent nucleosynthetic event would have to raise the ISM metallicity by a factor of $\gtrsim$50 from $[Fe/H] \sim -3.5$ to $[Fe/H] = -1.76 \pm 0.13$ without adding any N, Na, K, Sc, or Ba. Thus, the extremely low abundance of these elements implies that the majority of metals in J0931+0038 have to be made in "one shot," i.e., from a single nucleosynthetic event, rather than the continuous sum of multiple sources, as expected in ordinary chemical evolution. This is a conservative interpretation, because if the nucleosynthetic event produced any N, Na, K, Sc, or Ba, the ISM would have been even lower metallicity, possibly even primordial composition.

The presence of multiple extreme abundance ratios in J0931+0038 also favors a single source of elements, rather than combining multiple stellar sources. Each extreme ratio is erased by mixing with ordinary ISM, so invoking multiple element sources requires spatial and temporal coincidence, as the homogenization time in dwarf galaxies is only ∼100–300 Myr (see references in Ji et al. 2023). For example, it is tempting to invoke a Type Ia supernova in combination with a massive star supernova to explain the high metallicity, low odd–even, and unusual Fe-peak abundances (in analogy to the "iron-rich metal-poor stars"; Reggiani et al. 2023). The C–Ca and neutron-capture elements in J0931+0038 cannot come from the Type Ia supernova, so must instead originate from ISM material mixed with the Type Ia ejecta. However, this ISM would need to have one of the highest [Mg, Si, Ca/Fe] abundances ever observed, as well as simultaneously the highest [Sr, Y, Zr/Fe] abundances known. This is illustrated in Figure 3; of the elements shown, only Fe is produced in Type Ia supernovae so the horizontal red lines indicate the track of Type Ia supernova (SN) enrichment. If J0931+0038 originated from the shaded red [Fe/H] region and was enriched to high [Fe/H] by a Type Ia SN, it must have had the highest [Mg/Fe] and [Sr/Fe] ever observed. Thus, a Type Ia SN can only be invoked if it occurs simultaneously in the same region of a galaxy as an extreme CCSN that produced the high abundance of Mg, Sr, and other elements, which would be an implausible coincidence. A similar argument precludes most other combinations of multiple sources, though it may be plausible to combine two CCSNe that originate from the same binary system.

4.2. Maximum Metallicity of Supernova Models

An extraordinary nucleosynthetic event is needed to produce the high metallicity of J0931+0038 in one shot. We can constrain this by modeling the maximum metallicity achievable from stars forming directly out of a supernova explosion mixed with pristine gas. A supernova with a given explosion kinetic

Table 1
Chemical Abundances

Species	N	$\log \epsilon$	[X/H]	[X/Fe]	σ	$\Delta_{\rm NLTE}$
Li I	1	1.15	+0.10	+1.86	0.12	⋯
C–H	2	6.07	−2.49	−0.73	0.22	+0.10
N–H	1	5.36	−2.62	−0.86	Limit	−0.10
O I	3	7.23	−1.54	+0.22	0.17	−0.06
Na I	2	2.80	−3.49	−1.73	0.09	−0.10
Mg I	8	5.52	−2.03	−0.27	0.11	−0.02
Al I	1	4.15	−2.28	−0.52	0.50	+0.65
Si I	8	5.80	−1.79	−0.03	0.13	−0.17
K I	2	2.05	−3.09	−1.33	0.14	−0.20
Ca I	30	4.73	−1.64	+0.12	0.13	+0.02
Sc II	3	−0.06	−3.13	−1.37	0.09	⋯
Ti II	30	2.56	−2.38	−0.62	0.10	+0.12
V II	7	1.48	−2.41	−0.65	0.10	⋯
Cr II	5	3.75	−1.99	−0.23	0.12	⋯
Mn I	10	4.06	−1.46	+0.30	0.06	+0.34
Fe I	181	5.74	−1.76	+0.00	0.13	+0.11
Co I	4	3.37	−1.58	+0.18	0.10	+0.11
Ni I	26	5.04	−1.20	+0.56	0.15	+0.31
Cu I	1	2.64	−1.55	+0.21	0.19	+0.35
Zn I	2	3.17	−1.38	+0.38	0.08	⋯
Rb I	1	2.61	+0.09	+1.85	Limit	⋯
Sr II	3	1.85	−1.02	+0.74	0.07	+0.03
Y II	24	1.27	−0.94	+0.82	0.11	−0.00
Zr II	15	1.87	−0.71	+1.05	0.08	⋯
Nb II	1	1.34	−0.12	+1.64	Limit	⋯
Mo I	1	0.55	−1.33	+0.43	0.16	⋯
Ru I	1	0.68	−1.07	+0.69	0.14	⋯
Rh I	1	0.34	−0.57	+1.19	Limit	⋯
Pd I	1	0.46	−1.11	+0.65	0.14	⋯
Ag I	1	−0.15	−1.09	+0.67	Limit	⋯
Ba II	1	−2.33	−4.51	−2.75	0.13	+0.18
Eu II	1	−1.79	−2.31	−0.55	Limit	⋯

Note. The Magg et al. (2022a) solar normalization is used. NLTE corrections have already been applied and are shown for reference. For C and N, $\Delta_{\rm NLTE}$ is an estimate for the evolutionary correction. The correction listed is for each element's $\log \epsilon$, so [X/Fe] has an additional correction for [Fe/H] already applied. The abundance uncertainty for all elements is for the relative value [X/Fe], except for [Fe/H], which is the absolute metallicity uncertainty. Upper limits are denoted "Limit" in the σ column.

energy will sweep up a minimum mass of gas before the material can turn into stars (e.g., Cioffi et al. 1988; Ryan et al. 1996; Macias & Ramirez-Ruiz 2018; Ji et al. 2020b; Magg et al. 2020; Kolborg et al. 2022). This imposes an upper limit on [Fe/H]: it is possible to dilute the supernova metal yield into more gas, but not less.

To compare this to J0931+0038, we take the explosion energy and iron yield for a wide range of supernova nucleosynthesis models covering different progenitor masses, fallback, energies, and metallicities up to [Z/H] < -1.5 (Heger & Woosley 2002, 2010; Nomoto et al. 2013; Grimmett et al. 2018; Ebinger et al. 2020; shortened to HW02, HW10, NKT13, G18, and E20 within figure captions, respectively). We translate the explosion energy into a minimum gas mass using

$$M_{\rm dil,min} \approx 1.9 \times 10^4 M_\odot \, E_{51}^{0.96} n_0^{-0.11} \quad (1)$$

from Magg et al. (2020). Though this limit was derived assuming spherical symmetry and a homogeneous ISM, it was validated by cosmological radiation hydrodynamic simulations (Magg et al. 2022b). E_{51} is the kinetic energy in units of 10^{51} erg (or 1 B), and n_0 is the ISM density in units of cm^{-3}. Assuming a hydrogen mass fraction $X = 0.75$ and $A({\rm Fe})_\odot = 7.50$, the maximum metallicity achievable by a given supernova model and ISM density is given by

$$[{\rm Fe/H}] < -2.40 + \log \frac{M_{\rm Fe}}{0.1 M_\odot} - 0.96 \log E_{51} + 0.11 \log n_0. \quad (2)$$

This calculation assumes a homogeneous ISM, but inhomogeneous mixing tends to exacerbate the problem, as the denser gas that turns into stars is more resistant to metal pollution (Magg et al. 2020, 2022b).

We plot this maximum [Fe/H] with $n_0 = 1$ for several nucleosynthesis models in the top panel of Figure 4. The [Fe/H] of J0931+0038 is shown by a red shaded band, and it can only be achieved in extreme explosions of massive stars, either progenitor stars with $M > 50\ M_\odot$ or PISNe with initial mass $M \gtrsim 200\ M_\odot$. Less massive progenitors simply do not produce enough iron or dilute into a small enough hydrogen mass to explain the metallicity of J0931+0038. The one exception is an engine-driven supernova by Ebinger et al. (2020), which has $M_{\rm Fe} \sim 0.1\ M_\odot$ and energy $E \approx 0.3$ B. These models are the most self-consistent CCSN explosions shown, but they do not include any fallback from a reverse shock, which is estimated to be about 0.1 $M_\odot$ (Perego et al. 2015) and would substantially lower the maximum [Fe/H]. The other CCSN and HN models are exploded with parameterized models, where the explosion energy and mixing/fallback are varied freely or fixed to reproduce certain observations. At a fixed progenitor, higher explosion energies eject more Fe but dilute into more gas.[48]

4.3. Nucleosynthetic Origin

We searched through several grids of nucleosynthesis models to determine what type of supernova could explain the abundance pattern of J0931 + 0038. Here, we discuss the key element ratios that distinguish between progenitors, as illustrated in Figure 4. We primarily examine zero-metallicity supernova progenitors, as they have the largest range of model predictions, as well as lower neutron fractions that naturally result in a strong odd–even effect. However, we find no reason to exclude progenitors up to the ISM constraint [Fe/H] $\lesssim -3$ (Figure 3). Overall, the best models all invoke $M \gtrsim 50\ M_\odot$ progenitors, and the best match out of the current models is achieved by metal-free 80 $M_\odot$ HNe (Figure 5). However, we were unable to find any model that could explain all abundance features. A detailed discussion is given in Appendix B for nucleosynthesis experts.

We first reject electron-capture supernovae ($M \sim$ 8–10 $M_\odot$; Doherty et al. 2017; Wanajo et al. 2018), pulsational pair-instability supernovae ($100 \lesssim M/M_\odot \lesssim 140$; Woosley 2017), and general relativistic instability supernovae ($M > 10^4 M_\odot$; Chen et al. 2014) as possibilities. These all produce extremely high ratios of [C, N, O/Fe] inconsistent with J0931 + 0038.

We next examine deaths of 10–100 $M_\odot$ stars. We split these models into lower-energy CCSNe powered by the ordinary neutrino-driven mechanism ($E \lesssim 2$ B) and higher-energy HNe, which likely require extra energy from rotation and jets,

[48] This figure shows only a selection of zero-metallicity supernovae for clarity, but all models in these and other grids are shown in Appendix B.

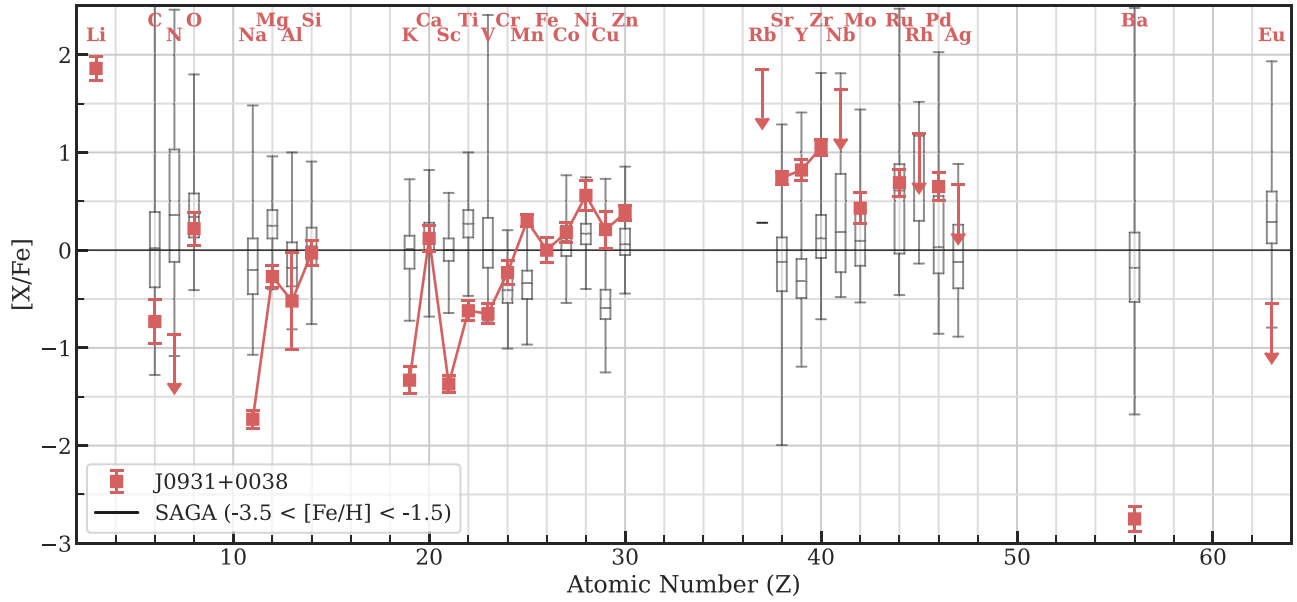

Figure 2. [X/Fe] (in NLTE when possible) vs. atomic number. The gray box plots for each element *X* are [X/Fe] from 4866 stars in the SAGA literature compilation (Suda et al. 2008) with $-3.5 < [\mathrm{Fe/H}] < -1.5$ to maximize the intrinsic [X/Fe] range. The SAGA abundances have been moved to the Magg et al. (2022a) abundance scale, and they have been shifted by the NLTE correction of J0931+0038 in Table 1. The box-and-whisker plots indicate the median and 25th–75th percentile with the box and the 1st–99th percentile with the whiskers. The abundances of Na, K, Sc, and Ba are among the lowest abundances of these elements ever measured. The uncertainty for Fe is the overall metallicity uncertainty, while for other elements, it is the precision relative to Fe. Note that the plotted Li value is [Li/Fe], and $A(\mathrm{Li}) = 1.15$.

perhaps driven by black hole accretion disks or millisecond magnetars (see references in Grimmett et al. 2021). It is broadly expected that 10–40 $M_\odot$ stars can explode as both CCSNe and HNe, while 40–100 $M_\odot$ stars probably need extra energy from an HN to explode, if they do at all (Heger et al. 2003; sixth row of Figure 4).[49] The most common supernovae with $M \lesssim 20\,M_\odot$ can be rejected due to their higher C/O yield ratios, a robust prediction of stellar evolution (Ishigaki et al. 2018; second row of Figure 4). Above 20 $M_\odot$, CCSNe eject large amounts of hydrostatically synthesized elements like O and Mg, resulting in high [Na/Mg] and [Mg/Fe] ratios that conflict with J0931 + 0038 (third and fourth rows of Figure 4). However, higher-energy explosions can reduce the [Na/Mg] and [α/Fe] yields to be consistent with J0931 + 0038 (see HN models from Grimmett et al. 2018 in Figure 4). Both CCSNe and HNe can likely synthesize the light neutron-capture elements seen in J0931 + 0038 through either neutrino-driven winds (Fröhlich et al. 2006; Bliss et al. 2018; Wanajo et al. 2018) or accretion disk winds (Pruet et al. 2004; Surman et al. 2006; Siegel et al. 2019), though it is hard to reproduce the exact pattern observed.

Overall, 40–100 $M_\odot$ HNe can broadly match most major abundance features of J0931 + 0038. The best match we found is an 80 $M_\odot$ 22 B model (Grimmett et al. 2018), shown in Figure 5. However, we emphasize that the full nucleosynthetic pattern is not fit by any existing model. In particular, the Fe-peak abundances are extremely difficult to explain; models must simultaneously produce low [Sc, Ti, V/Fe] (associated with lower energy) and high [Ni, Zn/Fe] (associated with higher energy) and high [Mn/Fe] (associated with high neutron fractions) but low odd–even ratios (associated with low neutron fractions). The higher-energy HNe with $E \gtrsim 10$ B that give the best matches to the nucleosynthesis pattern predict maximum metallicities $[\mathrm{Fe/H}] \ll -2$, strongly violating the metallicity constraint. Additionally, the low N and Ba restrict the progenitor's rotation, as rotational mixing increases N and would overproduce Ba through the *s*-process if there are seed nuclei (Ekström et al. 2008; Pignatari et al. 2008; Frischknecht et al. 2016; Choplin et al. 2018). This motivates considering other sources.

One intriguing possibility is that J0931 + 0038 was enriched by a PISN. Metal-free high-mass PISNe with $M \gtrsim 200\,M_\odot$ produce a very large amount of Fe, a strong odd–even effect, and low [α/Fe] ratios (Heger & Woosley 2002; Takahashi et al. 2018). These "smoking gun" signatures of PISNe qualitatively match J0931 + 0038. However, all existing PISN models produce negligible $[\mathrm{Zn/Fe}] < -1$ and no neutron-capture elements (Heger & Woosley 2002; Salvadori et al. 2019; fifth row of Figure 4). Thus, standard PISNe are unable to explain J0931 + 0038's abundance pattern. Still, the strong association with PISNe motivated some additional exploration, and we found that the intermediate neutron-capture (*i*-process) nucleosynthesis in PISN progenitors could be a promising mechanism. The *i*-process can occur if convection causes protons to be ingested into a He shell (Herwig et al. 2014; Woodward et al. 2015; Roederer et al. 2016; Banerjee et al. 2018; Clarkson et al. 2018), which generates neutrons that capture onto seed nuclei. With the right neutron exposure and initial composition (see Appendix B), the *i*-process converts Fe into enhanced Zn and Sr–Pd without significant Ba, which qualitatively matches J0931 + 0038. This explanation would require a metal-enriched PISN progenitor, implying that luminous PISNe could be found at later times than usually assumed (Hartwig et al. 2018). We show this speculative model in Figure 5, which simply adds the *i*-process pattern to a PISN yield.

[49] It is well known that the explosion landscape from 10 to 100 $M_\odot$ is not monotonic in initial mass, instead showing islands of explodability (e.g., Pejcha & Thompson 2015; Sukhbold et al. 2016; Burrows et al. 2018; Boccioli et al. 2023). However, due to reduced mass loss in metal-poor stars, current self-consistent models of neutrino-driven explosions have all stars above 40 $M_\odot$ collapsing to black holes (Ebinger et al. 2020).

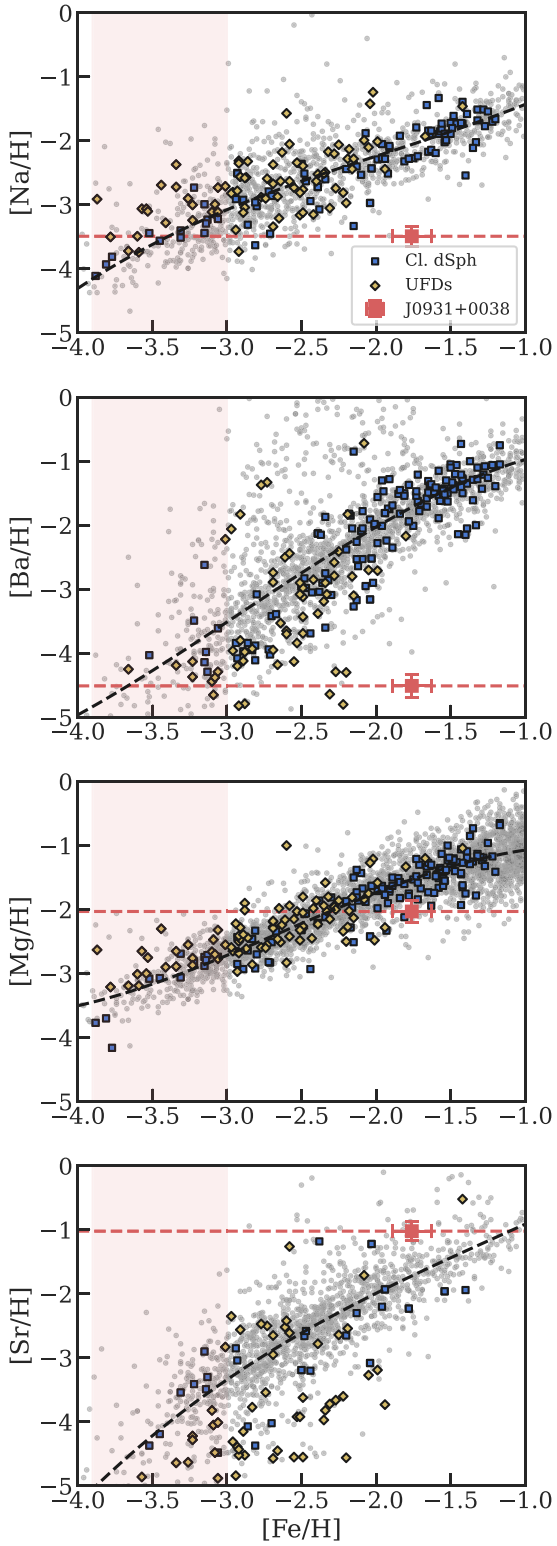

Figure 3. Composition of J0931+0038 (red square) for Na, Ba, Mg, and Sr compared to the SAGA database (gray points), higher-mass classical dwarf galaxies (blue squares), and lower-mass ultra-faint dwarf galaxies (yellow diamonds). The dashed black line is an outlier-clipped third-order polynomial fit to the SAGA data. The horizontal red line is the [X/H] of J0931+0038. In the top two panels, the red shaded region indicates [Fe/H] < -3, the ISM metallicity range that alone would contribute all of the Na, Ba, and other underabundant elements like N, K, and Sc observed in J0931+0038. The bottom two panels, Mg and Sr, show that explaining the low N, Na, K, Sc, and Ba by simply adding Fe (e.g., with a Type Ia supernova) would require extremely high abundances of other elements.

5. Conclusion

We have presented the extreme chemical abundance pattern of the star J0931 + 0038 (Figure 2). The low abundances of Na, K, Sc, and Ba and the high abundances of Fe-peak elements and Sr–Pd show that most of the metals in this star came from a single nucleosynthetic source (Figure 3). The high overall metallicity, low [C/O] ratio, and strong odd–even effect together combine to prefer progenitors with mass $> 50\,M_{\odot}$ (Figure 4). However, the detailed abundance pattern, especially in the iron peak, is not fully explained by any existing models of nucleosynthesis in massive stars (Figure 5). One possibility is the source might be a hypernova with a progenitor mass of $\sim 80\,M_{\odot}$, which would be the first example of an early supernova from a star with an initial mass between 50 and $100\,M_{\odot}$. Alternatively, the star might indicate *i*-process nucleosynthesis in the progenitor of a metal-enriched pair-instability supernova, which would be the first example of a metal-enriched pair-instability supernova. There may be other pathways that we did not consider.

J0931 + 0038 shows that current models of massive, metal-poor star nucleosynthesis are still quite limited, challenging the next generation of models. We suggest that J0931 + 0038 points to the inherent multidimensional nature of nucleosynthesis in massive stars, such as convective nuclear burning that likely impacts the iron peak yields (e.g., Herwig et al. 2014; Woodward et al. 2015; Curtis et al. 2019; Fields & Couch 2020; Burrows & Vartanyan 2021; Sieverding et al. 2023). We highlight rotation and jets for massive stars $\sim 80\,M_{\odot}$ and the *i*-process from proton ingestion in massive pair-instability supernova progenitors as fruitful paths for exploration. Another important consideration is binarity, as essentially all massive stars are in binaries, and most are in interacting binaries (Sana et al. 2012). There are still no studies of nucleosynthesis in metal-poor or metal-free supernovae of interacting binaries. This may be important especially because metal-poor stars do not lose much mass through winds, but they can lose significant mass through binary interactions (de Mink et al. 2008). To our knowledge, there also have been no studies of nucleosynthesis from interacting stars sufficiently massive for a pair-instability supernova, and it would be interesting to see if interactions could produce black hole or neutron star remnants that would remedy the deficiencies of single pair-instability supernova models. Finally, we note that whatever produces the abundance signature of J0931 + 0038 is probably very rare, otherwise this pattern would probably have already been previously discovered in the thousands of existing metal-poor stellar abundance data (Suda et al. 2008; Abohalima & Frebel 2018; Li et al. 2022). Converting this frequency to a volumetric rate estimate would require a model of dwarf galaxy and stellar halo formation, which is outside of the scope of this Letter.

Though we focused here on the nucleosynthetic implications, we speculate that J0931 + 0038's unique composition implies that the rare supernova events that could explain this signature should also be found in upcoming large transient surveys, such as Rubin/LSST (LSST Science Collaboration et al. 2009). If the chemical signature is due to an unusual pair-instability supernova, the heavy Fe-peak and neutron-capture elements point to the presence of a neutron star or black hole remnant involved in the explosion, which may result in unusual observational features of slowly evolving superluminous

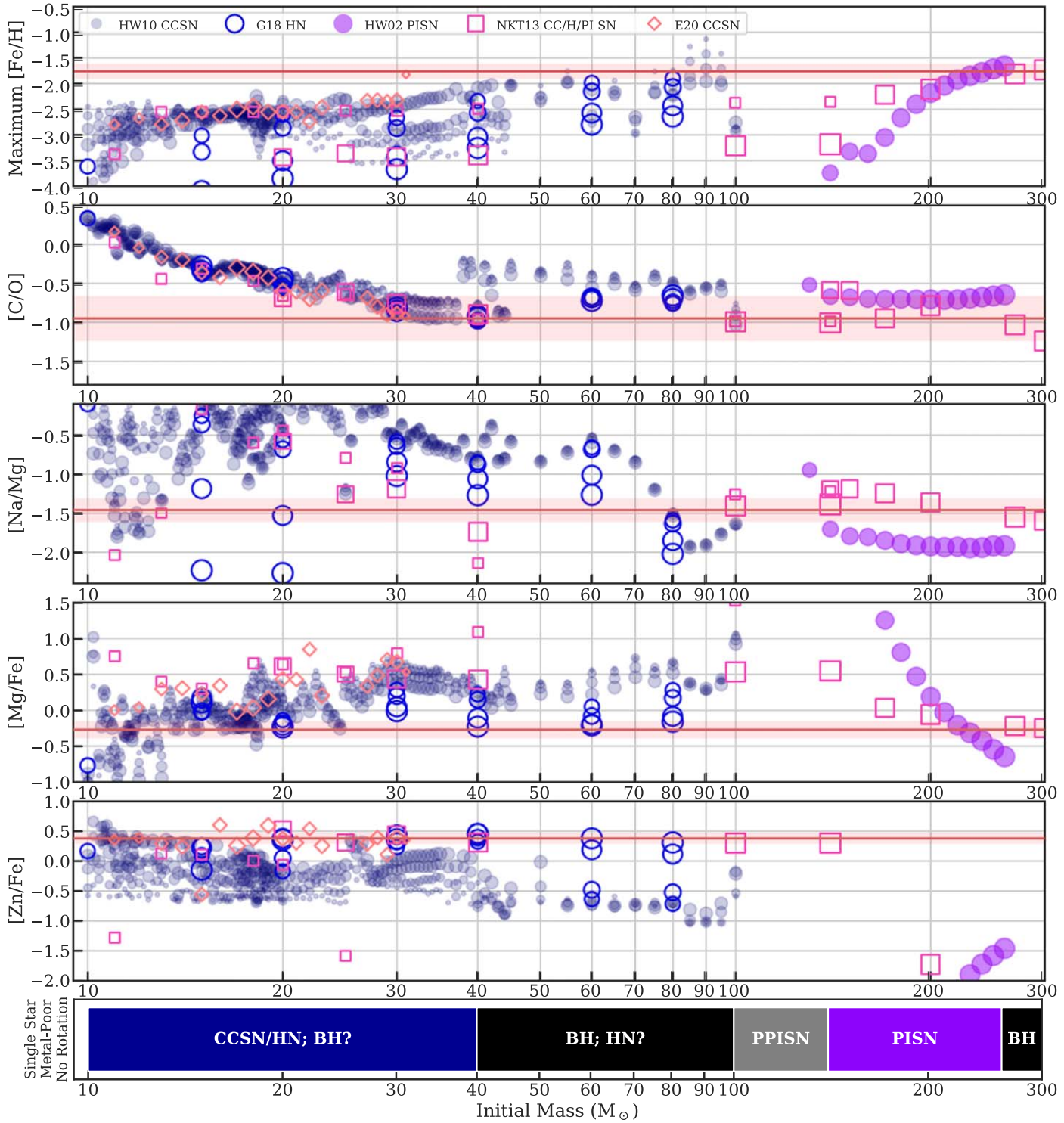

Figure 4. Initial mass vs. maximum [Fe/H], [C/O], [Na/Mg], [Mg/Fe], and [Zn/Fe] for zero-metallicity supernovae from five yield grids: CCSNe from HW10 (fiducial mixing, $E = 0.3$–2.4 B in steps of 2×), HNe from G18 (no mixing, $E = 5,\ 10,\ 50,\ 100$ B), PISNe from HW02, all types of supernovae from NKT13, and CCSNe from E20. Point sizes are proportional to log explosion energy (0.3–100 B). The horizontal red lines and shaded regions show the abundance of J0931 + 0038. First row: maximum [Fe/H] strongly prefers higher-mass progenitor stars with $M > 50\ M_{\odot}$. Larger explosion energies tend to synthesize more Fe but dilute into more H, with the balance indicated by vertical trends in point sizes. Second row: [C/O] rules out low-mass CCSNe ($M \lesssim 20\ M_{\odot}$). Third and fourth rows: [Na/Mg] and [Mg/Fe] disfavor intermediate-mass CCSNe (20–80 $M_{\odot}$). Higher-energy HNe match the abundances better and allow progenitors down to 40 $M_{\odot}$, but these all strongly violate the [Fe/H] constraint. E20 is removed from the [Na/Mg] plot, as the Na yields are not predicted. Fifth row: PISNe ($M > 140\ M_{\odot}$) are unable to produce significant Zn. Sixth row: estimated stellar fate given initial mass for a single, metal-poor, nonrotating star (HW02).

supernovae (Gal-Yam 2019; Nicholl 2021). If the chemical signature is instead due to a massive core-collapse supernova or hypernova, there should be supernovae of massive stars with low kinetic energy but relatively high ^{56}Ni luminosity (e.g., SN 2008ha; Foley et al. 2010; Moriya et al. 2010). Finally, if binarity is needed, it is possible that J0931 + 0038 has implications for features or outliers in the compact binary merger mass spectrum (Abbott et al. 2023; Farah et al. 2023).

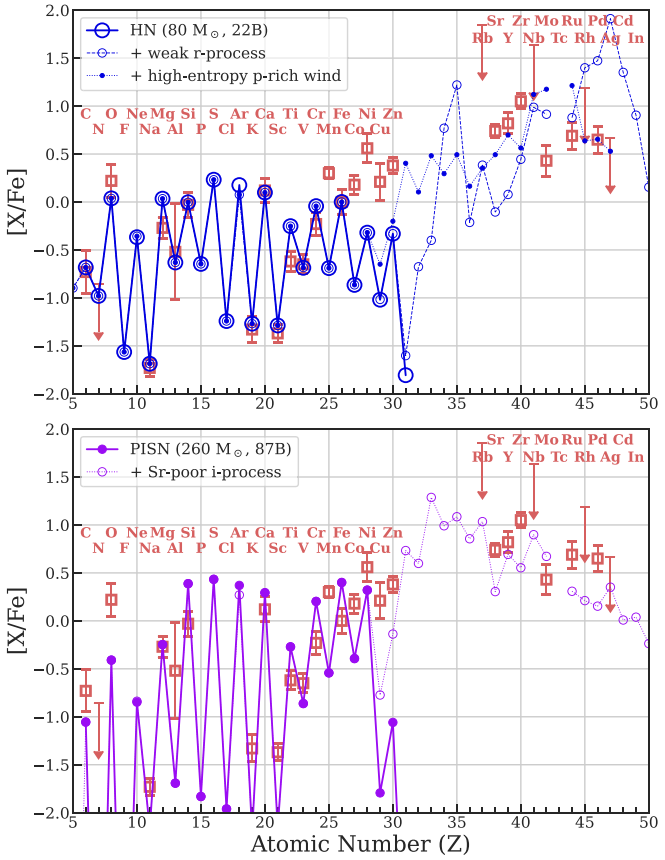

Figure 5. Representative best-matching nucleosynthesis models. Abundances of J0931 + 0038 are given as red squares with error bars. In the top panel, the large open blue circles connected by solid lines indicate the best-fit HN model (G18) The dotted blue line with small points and dashed blue line with small open circles indicate adding the HNe to a high-entropy proton-rich wind pattern (Bliss et al. 2018) and weak *r*-process pattern (Holmbeck et al. 2023), respectively. In the bottom panel, the filled purple circles with solid lines indicate the best-fit PISN model (HW02). The dotted purple line with small open circles indicates the same model with a modified *i*-process (calculated using the framework in Roederer et al. 2022; see Appendix B for details). The HN is the best fit to the lighter elements and has leeway to fit the heavier elements, but the high energy underpredicts [Fe/H]. The PISN easily matches the high [Fe/H], and we speculate that a full calculation of a metal-enriched PISN progenitor and explosion with *i*-process could remedy the disadvantages seen here.

J0931 + 0038 was identified in the first year of SDSS-V observing and after only one semester of follow-up of the metal-poor and low-α stars. The rapid discovery suggests that many more rare nucleosynthesis events like this should be found in the current and upcoming era of large spectroscopic surveys, and J0931 + 0038 emphasizes the importance of searching in multiple abundance dimensions rather than just at low metallicities. The unique chemical signature of J0931 + 0038 would also make it very easy to chemically identify companions from any accreted kinematic group. We searched for stars in APOGEE DR17 with similar kinematics and low Mg abundances from Horta et al. (2023) and examined all stars with low [Al/Mg] ratios that could potentially be analogs of this star. We were unable to find any candidates, but the current generation of large spectroscopic surveys may turn up future counterparts.

Acknowledgments

We acknowledge extremely helpful comments from the referee, Stan Woosley, that significantly improved the readability and clarity of this paper. This paper includes data gathered with the 6.5 m Magellan Telescopes located at Las Campanas Observatory, Chile. A.P.J. acknowledges the University of Chicago's Research Computing Center for their support. This work benefited from a workshop supported by the National Science Foundation under grant No. OISE-1927130 (IReNA), the Kavli Institute for Cosmological Physics, and the University of Chicago Data Science Institute. A.P.J. acknowledges Ani Chiti and Guilherme Limberg for helpful conversations. We acknowledge support awarded by U.S. National Science Foundation (NSF) grants AST-2206264 (A.P.J., P.T., S.A.U.), OISE-1927130 (IReNA; A.P.J., M.P.), PHY-1430152 (JINA-CEE; A.P.J., M.P.), AST-2303869 (AAPF; S.C.), and AST-2202135 (AAPF; E.J.G.). We acknowledge funding from the European Research Council (ERC) under several of the European Union's Horizon 2020 research and innovation programs: grant agreement Nos. 101008324 (ChETEC-INFRA; M.P.), 949173 (M.B.), 852839 (J.A., C.L.), and 833925 (STAREX; G.M.). A.H. was supported, in part, by the Australian Research Council (ARC) Centre of Excellence (CoE) for All Sky Astrophysics in 3 Dimensions (ASTRO 3D) through project No. CE170100013 and acknowledges software development support from Astronomy Australia Limited's ADACS scheme (Project IDs AHeger_2022B, AHeger_2023A) for the development of the StarFit code used here. M.P. is thankful for the support from the NKFI via K-project 138031 and the ERC Consolidator Grant (Hungary) program (RADIOSTAR, G.A. n. 724560). M.P. acknowledges the support to NuGrid from STFC (through the University of Hull's consolidated grant ST/R000840/1) and ongoing access to `viper`, the University of Hull High Performance Computing Facility. M.P. acknowledges the support from the "Lendület-2023" LP2023-10 Programme of the Hungarian Academy of Sciences (Hungary). M. B. is supported through the Lise Meitner grant from the Max Planck Society. We acknowledge support by the Collaborative Research center SFB 881 (projects A5, A10), Heidelberg University, of the Deutsche Forschungsgemeinschaft (DFG; German Research Foundation). H.R. acknowledges support from a Carnegie Fellowship. C.F. was supported by the United States Department of Energy, Office of Science, Office of Nuclear Physics (award No. DE-FG02-02ER41216).

Funding for the Sloan Digital Sky Survey V has been provided by the Alfred P. Sloan Foundation, the Heising-Simons Foundation, the National Science Foundation, and the Participating Institutions. SDSS acknowledges support and resources from the Center for High-Performance Computing at the University of Utah. The SDSS website is www.sdss.org.

SDSS is managed by the Astrophysical Research Consortium for the Participating Institutions of the SDSS Collaboration, including the Carnegie Institution for Science, Chilean National Time Allocation Committee (CNTAC) ratified researchers, the Gotham Participation Group, Harvard University, Heidelberg University, The Johns Hopkins University, L'Ecole polytechnique fédérale de Lausanne (EPFL), Leibniz-Institut für Astrophysik Potsdam (AIP), Max-Planck-Institut für Astronomie (MPIA Heidelberg), Max-Planck-Institut für Extraterrestrische Physik (MPE), Nanjing University, National Astronomical Observatories of China (NAOC), New Mexico State University, The Ohio State University, Pennsylvania State University, Smithsonian Astrophysical Observatory, Space Telescope Science Institute (STScI), the Stellar Astrophysics Participation Group,

Universidad Nacional Autónoma de México, University of Arizona, University of Colorado Boulder, University of Illinois at Urbana-Champaign, University of Toronto, University of Utah, University of Virginia, Yale University, and Yunnan University.

This work has made use of data from the European Space Agency (ESA) mission Gaia (https://www.cosmos.esa.int/gaia), processed by the Gaia Data Processing and Analysis Consortium (DPAC; https://www.cosmos.esa.int/web/gaia/dpac/consortium). Funding for the DPAC has been provided by national institutions, in particular the institutions participating in the Gaia Multilateral Agreement.

This research has made use of NASA's Astrophysics Data System Bibliographic Services, the arXiv preprint server operated by Cornell University, and the SIMBAD databases hosted by the Strasbourg Astronomical Data Center.

This research has made use of the Keck Observatory Archive (KOA), which is operated by the W. M. Keck Observatory and the NASA Exoplanet Science Institute (NExScI), under contract with the National Aeronautics and Space Administration.

Facilities: Sloan, Magellan:Clay (MIKE), Gaia

Software: `MOOG` (Sneden 1973; Sobeck et al. 2011), `Turbospectrum` (Plez 2012), `TSFitPy` (Gerber et al. 2023), `smhr` (Casey 2014; Ji et al. 2020a), `emcee` (Foreman-Mackey et al. 2013), `gala` (Price-Whelan 2017; Price-Whelan et al. 2022), `minesweeper` (Cargile et al. 2020), `dynesty` (Speagle 2020), `isochrones` (Morton 2015), `MultiNest` (Feroz & Hobson 2008; Feroz et al. 2009, 2019), `R` (R Core Team 2023), `StarFit` (Heger & Woosley 2010), `numpy` (van der Walt et al. 2011), `scipy` (Jones et al. 2001), `matplotlib` (Hunter 2007), `pandas` (Mckinney 2010), `seaborn` (Waskom et al. 2016), and `astropy` (Astropy Collaboration et al. 2013; Price-Whelan et al. 2018)

Appendix A
Observational Analysis Details

A.1. BOSS/MINESweeper Analysis

The SDSS-V BOSS (Gunn et al. 2006; Smee et al. 2013) spectra of J0931 + 0038 (Gaia DR3 3841101888330639872, ℓ, $b = 233.178248, +35.189507$) were observed on 2022 April 25, reduced using the BOSS data reduction pipeline (Bolton et al. 2012; Dawson et al. 2013; S. Morrison et al. 2024, in preparation), and analyzed using `MINESweeper` (Cargile et al. 2020), which performs a spectrophotometric fit simultaneously to the BOSS spectrum, the Gaia DR3 parallax (Brown et al. 2021), and all available broadband photometry (Gunn et al. 1998; Skrutskie et al. 2006; Mainzer et al. 2014; Chambers et al. 2016). Stars are constrained to lie on MIST isochrones (Choi et al. 2016), and stellar parameters are sampled using the `dynesty` nested sampling code (Speagle 2020). The spectroscopic fit was restricted to the region around Mg b (4750–5550 Å), as this is the region where the spectral models have been well calibrated for the H3 Survey (Conroy et al. 2019). `MINESweeper` provides the effective temperature, surface gravity, bulk metallicity, and [α/Fe] abundance based on this fit, where the α is primarily determined by the Mg b lines. The `MINESweeper` parameters and formal uncertainties for J0931 + 0038 were $T_{\rm eff} = 5220 \pm 30$ K, $\log g = 2.57 \pm 0.06$, [Fe/H] $= -1.9 \pm 0.1$, and [α/Fe] $= 0.03 \pm 0.17$.

The uniform `MINESweeper` analysis of all SDSS-V halo targets provides their 3D positions and velocities and enables investigation of their kinematics. The total specific energy was calculated using the latest `MilkyWayPotential2022` in `gala` (Price-Whelan 2017; Price-Whelan et al. 2022), which matches the rotation curve data from Eilers et al. (2019). The energy and three components of angular momentum of J0931 + 0038 are shown in Figure 6 as a large red star, compared to all other stars observed by the SDSS-V halo cartons from Internal Product Launch 2 as small black points. The energy and L_Z clearly show that J0931 + 0038 is a halo star, with an eccentric radial orbit ($e = 0.84$, pericenter = 1.1 kpc) consistent with the Gaia–Sausage–Enceladus (GSE) dwarf galaxy merger (Belokurov et al. 2018; Helmi et al. 2018). However, cosmological simulations suggest that this region of kinematic space is crowded, so the majority of metal-poor stars on GSE-like orbits actually do not come from GSE (Brauer et al. 2022; Orkney et al. 2023). Tailored GSE-like merger models also show that its debris is confined to a region $|L_x|$, $|L_y| \lesssim 800$ kpc km s^{-1} (Naidu et al. 2021; Amarante et al. 2022). Indeed, J0931 + 0038 lies outside the bulk of GSE stars in $L_X - L_Y$ space, which emphasizes the importance of checking multiple kinematic quantities when correlating halo structures. J0931 + 0038 is thus likely accreted as part of a now-disrupted dwarf galaxy but probably not the large GSE merger itself.

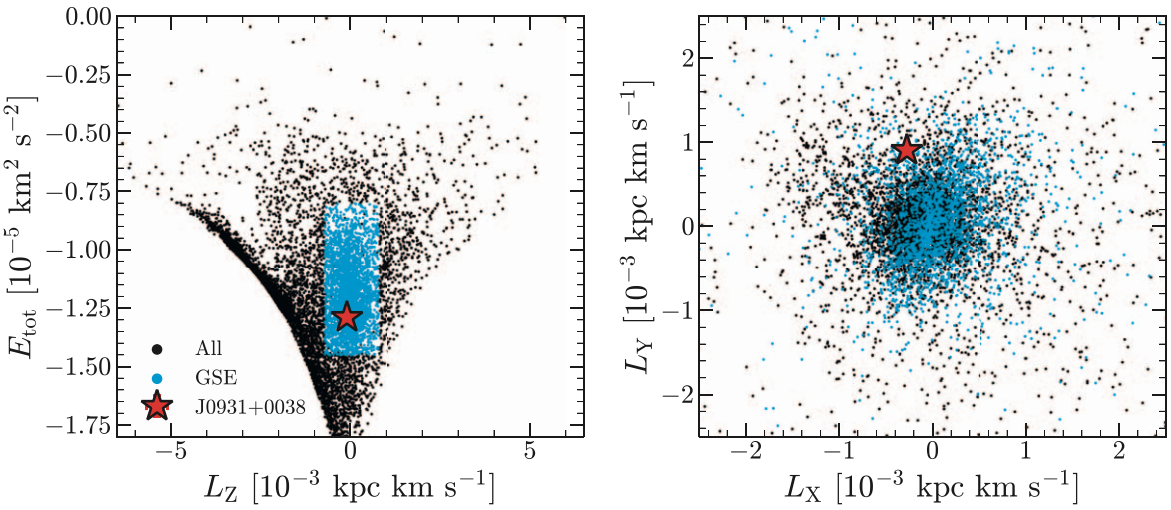

Figure 6. Kinematics of J0931 + 0038 (red star) compared to red giants observed by the SDSS-V halo program. Stars plausibly belonging to the GSE merger are highlighted in blue.

A.2. Stellar Parameters

Our analysis primarily used the 1D ATLAS model atmospheres (Castelli & Kurucz 2003) and the MOOG radiative transfer code (Sneden 1973) including scattering (Sobeck et al. 2011) and assuming LTE. The abundance analysis was conducted in the `smhr` environment (Casey 2014). The line lists and atomic data were selected from a combination of lines from Roederer et al. (2018) and Ji et al. (2020a), with atomic data adopted from linemake (Placco et al. 2021). Stellar parameters were determined using a combination of spectroscopy, photometry, isochrones, and Gaia parallax. We adopted an effective temperature of 5200 K based on the `MINESweeper` spectrophotometric results, then determined other parameters spectroscopically. The surface gravity required to balance the neutral and ionized iron abundances was $\log g = 2.75$, and the microturbulence required to balance the Fe II line abundances was 1.65 km s^{-1}, with a model metallicity of -1.9 and using solar-scaled abundances for the ATLAS atmosphere composition ($[\alpha/\mathrm{Fe}] = 0$).

Stellar parameters and uncertainties were checked using two independent fits to the spectral energy distribution (SED) and parallax. First, we performed an analysis of the broadband SED of the star together with the Gaia DR3 parallax (with a systematic offset applied; see, e.g., Stassun & Torres 2021) following the procedures described in Stassun & Torres (2016) and Stassun et al. (2017, 2018). We pulled the JHK_S magnitudes from the Two Micron All Sky Survey (2MASS), the W1–W3 magnitudes from the Wide-field Infrared Survey Explorer, the $G_{\rm BP}$ and $G_{\rm RP}$ magnitudes from Gaia, the *grizy* magnitudes from Pan-STARRS, and the near-UV (NUV) magnitude from the Galaxy Evolution Explorer (GALEX). We also used the Gaia spectrophotometry spanning 0.4–1.0 μm. Altogether, the available photometry spans the full stellar SED over the wavelength range 0.2–10 μm. The GALEX flux in particular helps to constrain the metallicity, and the Gaia spectrophotometry provides an especially strong constraint on the overall absolute flux calibration. We then performed a fit using PHOENIX stellar atmosphere models (Husser et al. 2013), with the free parameters being the effective temperature ($T_{\rm eff}$) and metallicity ([Fe/H]), as well as the extinction, which we set to the maximum line-of-sight value $A_V = 0.15 \pm 0.02$ from the Galactic dust maps of Schlegel et al. (1998) due to the system's large distance. We initially assumed a surface gravity of $\log g \approx 2.5$ given the likely evolutionary state of the star. The resulting fit has a best-fit $T_{\rm eff} = 5250 \pm 50$ K and $[\mathrm{Fe/H}] = -2.3 \pm 0.3$. Integrating the (unreddened) model SED gives the bolometric flux at Earth, $F_{\rm bol} = 7.988 \pm 0.092 \times 10^{-11}$ erg s^{-1} cm^{-2}. Taking the $F_{\rm bol}$ and $T_{\rm eff}$ together with the Gaia parallax gives the stellar radius, $R_\star = 8.65 \pm 0.9\ R_\odot$. In addition, we estimate the stellar mass to be $M_\star = 0.8 \pm 0.1\ M_\odot$, as J0931 + 0038 is a metal-poor old red giant. The mass and radius together confirm $\log g \approx 2.5$.

Second, we also derived the stellar parameters of J0931 + 0038 using the `isochrones` (Morton 2015) package to execute with `MultiNest` (Feroz & Hobson 2008; Feroz et al. 2009, 2019) a simultaneous Bayesian fit of the MIST isochrone grid (Paxton et al. 2011, 2013, 2018, 2019; Choi et al. 2016; Dotter 2016; Jermyn et al. 2023) to a curated collection of data for the star. We fit (1) GALEX GUVcat_AIS NUV (Bianchi et al. 2017), SDSS DR18 *ugiz* (Fukugita et al. 1996; Gunn et al. 1998; York et al. 2000; Doi et al. 2010; Abdurro'uf et al. 2022), Gaia DR2 *G* (Gaia Collaboration et al. 2016; Arenou et al. 2018; Evans et al. 2018; Gaia Collaboration et al. 2018; Riello et al. 2018), 2MASS JHK_s (Skrutskie et al. 2006), and Wide-field Infrared Survey Explorer CatWISE2020 *W1W2* photometry (Wright et al. 2010; Marocco et al. 2021); (2) a zero-point-corrected Gaia DR3 parallax (Lindegren et al. 2021a, 2021b; Fabricius et al. 2021; Gaia Collaboration et al. 2021; Rowell et al. 2021; Torra et al. 2021); and (3) an estimated reddening value based on a 3D reddening map (Green et al. 2014, 2019). We use a log-uniform age prior between 8.0 and 13.7 Gyr, a uniform reddening prior between the estimated reddening value minus/plus five times its uncertainty, and a distance prior proportional to the volume between the Bailer-Jones et al. (2021) geometric distance minus/plus five times its uncertainty. We find the photospheric stellar parameters $T_{\rm eff} = 5140^{+20}_{-10}$ K, $\log g = 2.51^{+0.07}_{-0.07}$, and $[\mathrm{Fe/H}] = -1.63^{+0.07}_{-0.01}$.

As discussed in the main text, we adopted stellar parameters of $T_{\rm eff} = 5200 \pm 100$ K, $\log g = 2.75 \pm 0.20$, $\nu_t = 1.65 \pm 0.3$ km s^{-1}, $[\mathrm{M/H}] = -1.9 \pm 0.1$, and $[\alpha/\mathrm{Fe}] = 0.0$. The temperature uncertainty of 100 K resulted in correlated $\log g$ and metallicity offsets of 0.20 and 0.1 dex. The microturbulence uncertainty of 0.3 km s^{-1} is very conservative and represents the most extreme values found during line strength balance in both LTE and NLTE in all permutations. These were later propagated into all abundance uncertainties.

A.3. LTE Abundance Analysis

Chemical abundances were determined in 1D LTE using MOOG and ATLAS in `smhr`, with a mix of equivalent widths for isolated, unblended lines and syntheses for molecular bands, lines with hyperfine structure, or moderately blended lines. The local continuum and smoothing were allowed to vary for each feature. Syntheses were fit by minimizing a chi-square statistic (for more details, see Ji et al. 2020a). The final chemical abundance for each species was found as the unweighted average of individual line abundances. The Fe in [X/Fe] refers to Fe I. For nondetections, we synthesize a best-fit spectrum with no line, then calculate a formal 5σ upper limit by increasing the abundance until the χ^2 changes by 5^2. This assumes no uncertainties in the continuum, which is a good assumption given the high S/N of our spectrum, except for the N–H molecule, where we visually estimated a very conservative upper limit for N–H (formally $> 10\sigma$) with a synthetic spectrum.

Systematic abundance uncertainties due to stellar parameters were found by redetermining the chemical abundances at two alternate stellar parameter values based on the stellar parameter uncertainty: ($T_{\rm eff}$, $\log g$, ν_t, [M/H]) = (5100 K, 2.55, 1.65, -2.0) and (5200 K, 2.75, 1.95, -1.9). For Fe I, we sum the total difference in [Fe I/H] in quadrature for these two sets of stellar parameters and adopt that as the stellar parameter uncertainty on the absolute metallicity of the star. For species other than Fe I, we adopt the difference in [X/Fe I] for each of these variations as the stellar parameter uncertainty and sum them in quadrature. The latter accounts for the fact that [X/H] and [Fe/H] are highly correlated with respect to stellar parameters, so the relative abundance uncertainty is smaller (which is the relevant uncertainty when considering the total abundance pattern).

To investigate the systematic effect of our model atmosphere, line list, and radiative transfer code, we also analyzed a subset of the lines using 1D spherical MARCS model atmospheres (Gustafsson et al. 2008), the most recent version of

Turbospectrum in TSFitPy (Plez 2012; Gerber et al. 2023), and a line list from Gaia-ESO (Heiter et al. 2021) with gaps filled and the range further extended with VALD (Kupka et al. 1999). We adopt the MARCS model atmospheres, and the analysis used slightly different stellar parameters: $T_{\rm eff} = 5200$ K, $\log g = 2.60$, $\nu_t = 1.6\,{\rm km\,s^{-1}}$, [Fe/H] $= -1.85$, and [α/Fe] $= +0.4$ (due to the standard MARCS grid). The final LTE abundance differences are all within 0.1 dex, with the exception of aluminum, which will be discussed later. We thus decided to adopt a minimum 0.1 dex systematic uncertainty per line, such that the total systematic uncertainty goes down as the square root of the number of lines.

In summary, the adopted abundance uncertainty is the quadrature sum of four components: the line-to-line standard deviation for a given species, a minimum systematic of 0.1 dex divided by the square root of the number of lines per element, the stellar parameter error after changing $T_{\rm eff}$ and $\log g$ with their correlated uncertainties, and the stellar parameter error after changing ν_t by 0.3 $\rm km\,s^{-1}$.

A.4. NLTE Corrections

NLTE corrections for most elements were determined using TSFitPy (Gerber et al. 2023). We fit the same lines used for the MOOG/ATLAS analysis but restricted to the wavelength range 3700–9200 Å using the Gaia-ESO line list with gaps filled and the range extended using the VALD line list. The NLTE corrections were determined using the standard concept of the NLTE abundance correction (Bergemann & Nordlander 2014), which represents the difference in abundance that is required to match the equivalent width of an NLTE model line to that of the LTE line computed using the identical values of stellar parameters. The elements and model atom references were oxygen (Bergemann et al. 2021), sodium (Larsen et al. 2022), magnesium (Bergemann et al. 2017), silicon (Bergemann et al. 2013; Magg et al. 2022a), calcium (Mashonkina et al. 2017; Semenova et al. 2020), titanium (Bergemann 2011), manganese (Bergemann et al. 2019), iron (Bergemann et al. 2012b; Semenova et al. 2020), cobalt (Bergemann et al. 2010; Yakovleva et al. 2020), nickel (Bergemann et al. 2021; Voronov et al. 2022), strontium (Bergemann et al. 2012a; A. Gallagher et al. 2024, in preparation), yttrium (Storm & Bergemann 2023), and barium (Gallagher et al. 2020). The average NLTE correction from all lines was taken as the total NLTE correction for that element.

A few elements are not currently included in TSFitPy, and we describe their NLTE corrections below.

Aluminum. Only the 3961 Å line is usable, and it is heavily blended with a strong Ca and H feature. The abundance of Al is extremely uncertain as a result. We measure [Al/Fe] in LTE through spectrum synthesis, and the LTE abundances from MOOG and TSFitPy differed by 0.2 dex, likely dominated by treatment of the blending Ca and H feature. We then adopt the NLTE correction from the grid of Nordlander & Lind (2017) to get a +0.65 dex correction to [Al/Fe]. Preliminary calculations with other unpublished Al model atoms in TSFitPy suggested a smaller correction of +0.33 dex. We thus adopt a very large uncertainty of 0.5 dex for the Al abundance to represent both the blending and NLTE correction uncertainty.

Potassium. The K abundance is derived from equivalent widths of the 7699 and 7665 Å lines, which are both unaffected by telluric lines in this star. Examining stars with similar stellar parameters in Reggiani et al. (2019), NLTE corrections for K from the 7699 line range from −0.17 to −0.24 dex. We adopt a −0.2 dex correction and increase the K uncertainty by adding 0.1 dex in quadrature.

Copper. We use the equivalent width of the 5105 Å line and adopt an empirical correction of +0.35 dex from Roederer & Barklem (2018). This matches the theoretical calculations (Andrievsky et al. 2018; Korotin et al. 2018), and we increase the uncertainty by adding 0.15 dex in quadrature to reflect the scatter from the theoretical calculations.

Elements without corrections. Roederer et al. (2022) provide a detailed accounting of what corrections might be expected based on comparisons of neutral and ionized lines in star HD 222925 with [Fe/H]= − 1.5 and $T_{\rm eff} = 5640$ K. Based on this, we do not expect significant NLTE corrections for zinc, zirconium, molybdenum, or ruthenium, while possible NLTE corrections for rhodium and palladium are unconstrained.

A.5. Evolutionary State Corrections

J0931 + 0038 has $\log g = 2.75$, so it has passed the first dredge-up but not the red giant branch bump, and a small amount of C is converted to N. To account for this difference, we examined metal-poor red giants in APOGEE DR17 with [Fe/H] < -1.5. Stars after the first dredge-up have [C/N] higher by 0.2 dex, where [C/Fe] is lower by 0.1 dex and [N/Fe] is higher by 0.1 dex. For J0931 + 0038, we thus increase [C/H] by +0.1 dex, decrease the [N/H] upper limit by −0.1 dex, and increase each element's uncertainty by adding 0.2 dex in quadrature.

We also measured a Li abundance of $A({\rm Li}) = 1.15 \pm 0.12$. Given the $\log g$ of this star, this Li abundance is consistent with Li depletion in the first dredge-up (e.g., Tayar & Joyce 2022), a good independent check on the stellar parameters.

A.6. Binarity and Photometric Variability

J0931 + 0038 displays no evidence for a present-day binary companion. The heliocentric radial velocity for MIKE was found to be $105.5 \pm 0.4\,{\rm km\,s^{-1}}$ (measured with the method in Ji et al. 2020b), while Gaia DR3 RVS reports $104.3 \pm 4.0\,{\rm km\,s^{-1}}$. These velocities are consistent within uncertainties. The velocity scatter from multiple Gaia RVS transits is large but typical for stars of similar spectral type, distance, and signal-to-noise ratio (Chance et al. 2022), and there is no evidence for excess astrometric scatter (Penoyre et al. 2020).

Photometric variability could also be used to identify binary companions or measure solar-like oscillations. J0931 + 0038 does not show up in Hon et al. (2021) as a solar-like oscillator. We obtained the TESS light curve of J0931 + 0038 (TIC 383218318) using TESScut (Brasseur et al. 2019) with a custom aperture and subtracting background flux. Following Avallone et al. (2022), we normalized and smoothed each of the sectors and took a Fourier transform of the resulting light curve. We do not see any evidence of periodic variability in the TESS light curve that would suggest detectable rotational modulation or oscillations, though J0931 + 0038 is relatively faint for TESS and has a limited time baseline.

A.7. Comparison to Notable Stars

Figure 7 shows the [X/Fe] of J0931 + 0038 compared to four notable stars: three HN candidate stars with varying neutron-capture element abundances, HE 1327−2326

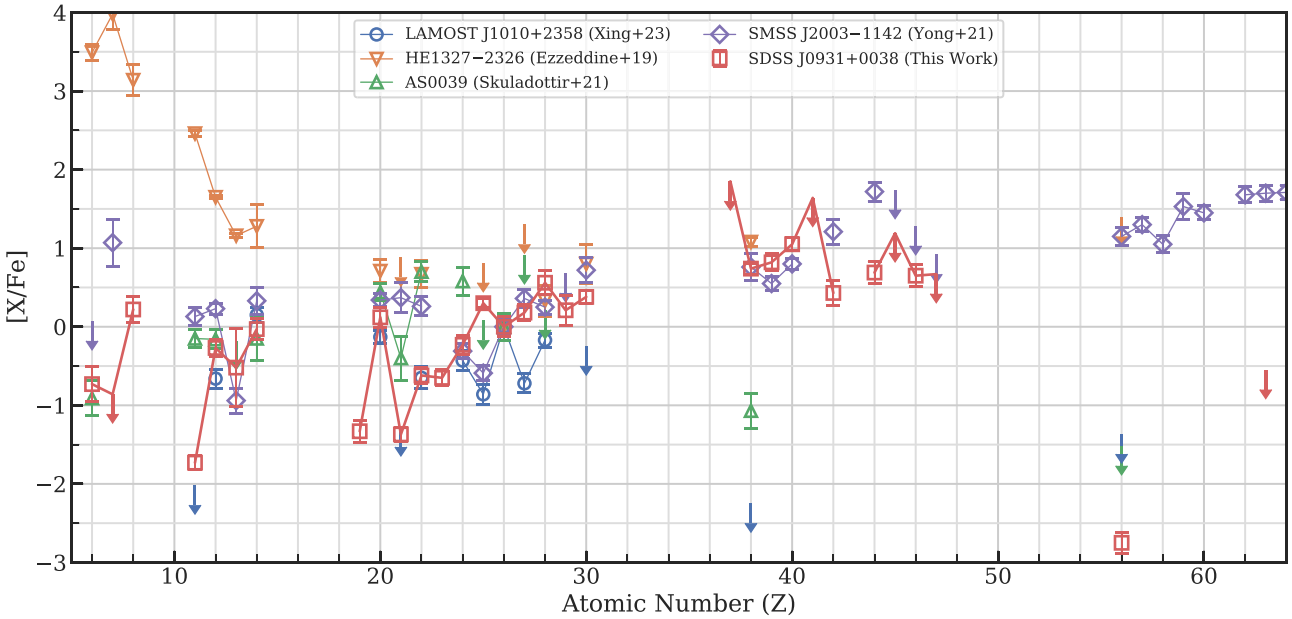

Figure 7. Chemical abundances of J0931 + 0038 compared to four other notable stars. LAMOST J1010 + 2358 has a pure signature of a PISN, while the other three are metal-poor stars whose compositions are currently best explained with HN models.

(Frebel et al. 2005; Ezzeddine et al. 2019), SMSS J2003 −1142 (Yong et al. 2021), and AS 0039 (Skúladóttir et al. 2021), and the PISN star J1010 + 2358 (Xing et al. 2023; though note that it has recently been argued that this star is also consistent with an extreme CCSN; Jeena et al. 2023).

It is clear that J0931 + 0038 has an extreme abundance pattern even compared to these other notable stars. Because of its relatively high metallicity, it is also easier to measure many more elements. The clear signature is that the odd elements Na, Al, K, and Sc (Z = 11, 13, 19, and 21) in J0931 + 0038 are lower than almost all the other stars, with the exception of the PISN star J1010 + 2358. The carbon and oxygen abundances (Z = 6 and 8) are relatively low, in contrast with more metal-poor stars that tend to be carbon-enhanced, like HE 1327 −2326 and SMSS J1605−1443. Mn (Z = 25) is unusually high, as nearly all metal-poor stars have [Mn/Fe] < 0. Co through Zn (Z = 27–30) are also elevated, which is usually associated with HNe (Ezzeddine et al. 2019; Yong et al. 2021).

The three literature HN stars have very different neutron-capture patterns. HE 1327−2326 has high Sr (Z = 38) but no Ba (Z = 56), attributed to an aspherical HN (Ezzeddine et al. 2019). SMSS J2003−1142 has a full *r*-process pattern from Sr to Eu (and beyond), attributed to a magnetorotationally driven HN (Yong et al. 2021). AS 0039 is a star in the Sculptor dwarf galaxy also suggested to be consistent with a high-energy but spherical HN, and it has very low Sr and Ba (Skúladóttir et al. 2021). It appears that HNe are able to generate a whole range of neutron-capture nucleosynthesis, as might be expected based on potentially variable strengths of the central engine. Our star J0931 + 0038 has a full complement of first neutron-capture peak elements from Sr to Pd and nothing beyond, which makes it most similar to HE 1327−2326's much sparser abundance pattern. Note that the pattern is flat in [X/Fe], which differs substantially from the "pure" *r*-process pattern in SMSS J2003 −1142, as well as theoretical *r*-process predictions (Holmbeck et al. 2023).

A.8. Comparison to Typical Metal-poor Stars

As a complement to Figures 2 and 3, Figure 8 shows [Fe/H] versus [X/H] for 21 elements. The gray points are halo stars from the SAGA database (Suda et al. 2008), and blue and yellow points are an extended dwarf galaxy compilation from JINAbase (Abohalima & Frebel 2018). The literature abundances have been shifted by the NLTE and evolutionary corrections from Table 1. We show the one-to-one line ([X/Fe] = 0) as a dotted black line and an outlier-clipped polynomial fit to the SAGA abundances as a dashed black line (best fit indicated on each panel), which represents the typical ISM composition at any given metallicity. At its [Fe/H], J0931 + 0038 is a visible low outlier in the Na, Al, K, Sc, Ti, V, Ba, and Eu panels while simultaneously being a high outlier in Mn, Co, Ni, Cu, Zn, and Sr.

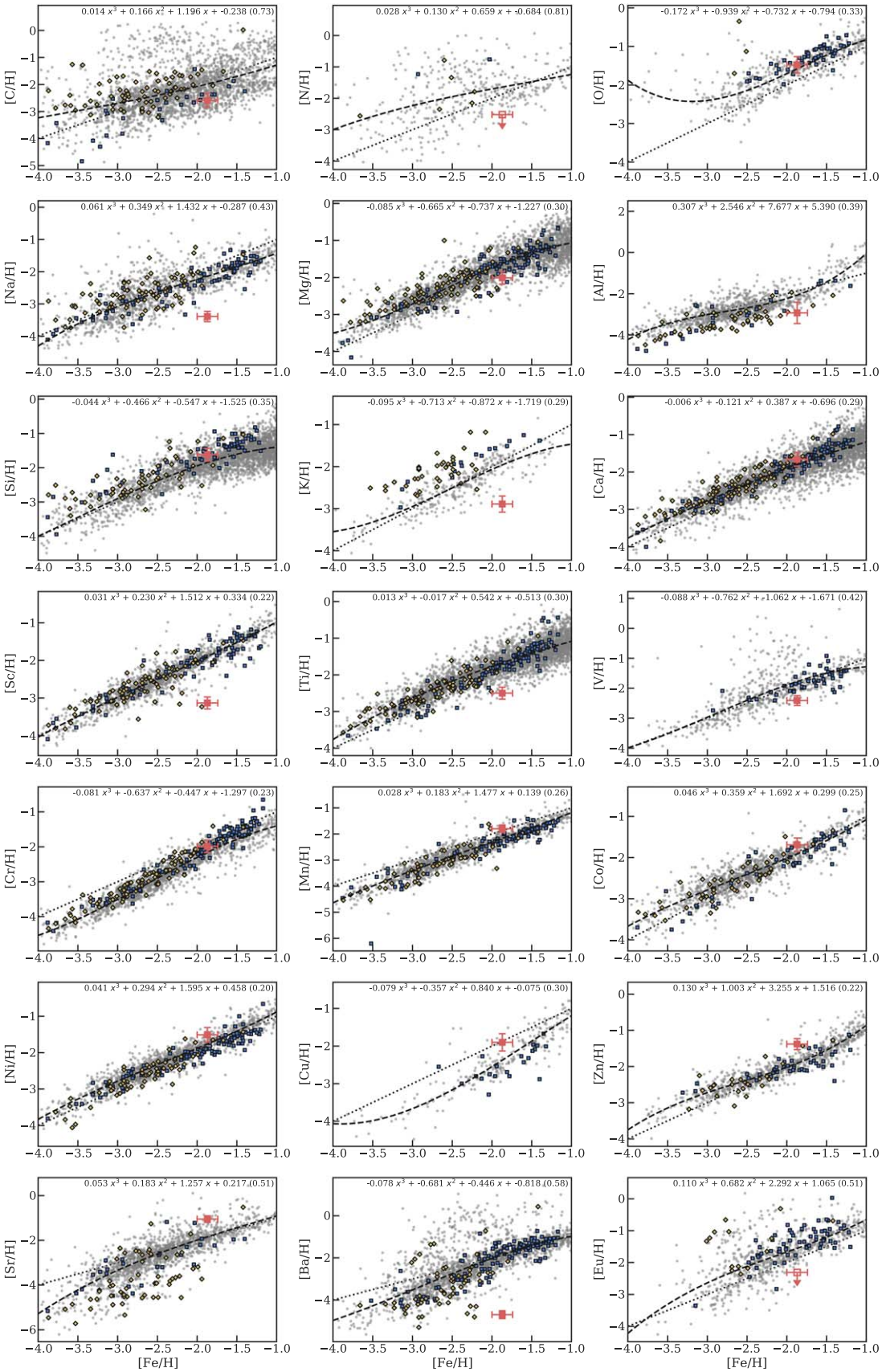

Figure 8. [X/H] vs. [Fe/H] for SAGA (gray points) and dwarf galaxy stars (blue is classical dSph, yellow is ultra-faint dwarf). J0931 + 0038 is shown as a large red square. The dotted line indicates [X/Fe] = 0, and the dashed line is the best fit to the SAGA stars that we use as an empirical ISM composition. Note that the comparison abundances have been shifted by the NLTE and evolutionary corrections for J0931 + 0038.

Appendix B
Nucleosynthesis Origin

We performed an extensive literature search for nucleosynthesis predictions that could match J0931 + 0038. In this section, we will mostly ignore the metallicity constraint from J0931 + 0038 (Section 4.1) and instead focus on what sites or conditions could produce the observed abundance pattern.

B.1. Brief Nucleosynthesis Summary

We start by briefly summarizing some key element ratios and the main physics of the supernova progenitor and explosion that drives their values, discussing them in the context of J0931 + 0038.

1. The [C/O] value is a good indicator of the zero-age main-sequence (ZAMS) mass of the progenitor, where a lower value indicates a more massive star (e.g., Ishigaki et al. 2018). The low [C/O] value of J0931 + 0038 is typically found for yields of massive progenitors with ZAMS mass $\gtrsim$20 $M_{\odot}$ (Heger & Woosley 2010; Nomoto et al. 2013). We note that this ratio and the overall products of carbon burning are subject to uncertainties in the $^{12}C(\alpha,\gamma)^{16}O$ rate and the treatment of convection (e.g., Imbriani et al. 2001; El Eid et al. 2004; deBoer et al. 2017; Farmer et al. 2019). Additionally, binary interactions may affect [C/O] predictions, though current models in solar metallicity stars suggest that interactions increase C yields (Farmer et al. 2021, 2023).
2. [N/O] can potentially help constrain rotation in the progenitor, as nitrogen is typically enhanced in rotating stars (e.g., Choplin et al. 2018). However, while J0931 + 0038 has a very low upper limit on the abundance of nitrogen, we found that it is insufficient to rule out rotating metal-poor progenitors, as the large N enhancement would still be below our detection threshold (Ekström et al. 2008; Limongi & Chieffi 2018).
3. The extreme odd–even effect seen for elements from C to Sc, characterized by low values of [Na/Mg] and [K/Ca], occurs in stars with low neutron fractions. Such values are typically associated with PISNe (Heger & Woosley 2002; Kozyreva et al. 2014; Takahashi et al. 2018) but also occur to a lesser extent in any massive zero- or low-metallicity progenitor (Heger & Woosley 2010; Nomoto et al. 2013; Limongi & Chieffi 2018). The low [Na/Mg] especially prefers higher initial mass progenitors with $M > 70\,M_{\odot}$. Rotation can "fill in" the odd elements as well (e.g., Choplin et al. 2018).
4. The low alpha abundances, e.g., [Mg/Fe], indicate a low ratio of hydrostatic to explosively synthesized elements, which tends to occur either in lower-mass CCSN progenitors ($\lesssim$15 $M_{\odot}$; McWilliam et al. 2013; Carlin et al. 2018) or in the most massive PISNe (Heger & Woosley 2002; Salvadori et al. 2019).
5. The composition of the iron group from Sc to Zn depends sensitively on the details of the supernova explosion, such as explosion energy, remnant mass, convection, jets, and more. All of these elements are produced during explosive silicon burning, with different degrees of contribution from complete and incomplete burning and likely important 3D effects (e.g., Curtis et al. 2019; Sieverding et al. 2023). J0931 + 0038 has an unusual iron group composition, showing very low [Sc, Ti, V/Fe] along with high [Mn, Ni, Zn/Fe]. We were unable to find any existing supernova yield model matching the whole Fe-peak pattern.
6. The elements from Sr and heavier are formed primarily through the slow (*s*) and rapid (*r*) neutron-capture processes, though proton-capture and *i*-processes are possible as well. In J0931 + 0038, the very low [Ba/Fe] rules out a strong, neutron-rich *r*-process (e.g., from neutron star mergers; Holmbeck et al. 2023) and the main *s*-process (e.g., Lugaro et al. 2012). Most remaining scenarios to explain the high [Sr–Pd/Fe] invoke nucleosynthesis associated with the formation of neutron stars or black holes, with the *i*-process activated in external He-rich layers as an alternative.

In Figures 9 (light elements) and 10 (Fe-peak elements), we show plots of all the key element ratios with respect to progenitor initial mass and explosion energy for eight models that span the range of predictions: primordial supernovae from Heger & Woosley (2002), Heger & Woosley (2010), Limongi & Chieffi (2012) (LC12), Nomoto et al. (2013, shortened to N13 in figure captions), Grimmett et al. (2018), and Ebinger et al. (2020) and low-metallicity supernovae from Limongi & Chieffi (2018, shortened to LC18 in figure captions; including rotation and keeping the most massive stars that may not explode), Ritter et al. (2018, shortened to R18 in figure captions), Notomo et al. 2013, and Ebinger et al. 2020. We somewhat arbitrarily put a line at 2.5 B to split models between CCSNe and HNe. We cut models to only those with metallicity < -1.5 solar. Note that the models by Limongi & Chieffi (2012), Limongi & Chieffi (2018), and Ritter et al. (2018) do not have explosion energies provided, so we do not include those on the explosion energy figures, and the progenitor models in Ebinger et al. (2020) did not include odd elements, so we removed it from the N and Na panels for Figure 9. The horizontal red lines and shaded regions indicate the observed value and uncertainty in J0931 + 0038, including an upper limit for [N/O].

The comparison between these figures and J0931 + 0038 is qualitatively summarized by Table 2. Check marks are given when nearly all models in a particular category can match J0931 + 0038. We use a check mark with a question mark if existing models would work, but we felt there were large theoretical uncertainties or important exceptions. Crosses indicate that current theoretical models suggest a particular criterion is impossible for some category of models. A cross with a question mark indicates that most models do not satisfy the criterion, but we felt there were large theoretical uncertainties and/or large variations in existing predictions. The "rapid rotation" column uses the LC18 conclusions, though the behavior could potentially change in other models. Overall, we can see that the 50–100 $M_{\odot}$ HN column has no observation fully ruling it out, although there are substantial uncertainties. The massive PISN column has the most check marks, but it is solidly ruled out by the Fe-peak and neutron-capture elements. (The neutron-capture elements will be discussed more in Appendix B.4.)

A few rows in Table 2 merit more discussion. We originally expected the low [N/O] limit to substantially constrain rotation velocities or initial masses (Meynet et al. 2006; Ekström et al. 2008; Placco et al. 2016), but it turns out that since [N/O] is so low in most metal-free supernovae, even a 100× increase is not that constraining. However increased rotation does substantially impact [Na/Fe], as well as all the odd Fe-peak elements. It is also strongly constrained by the low Ba, since the *s*-

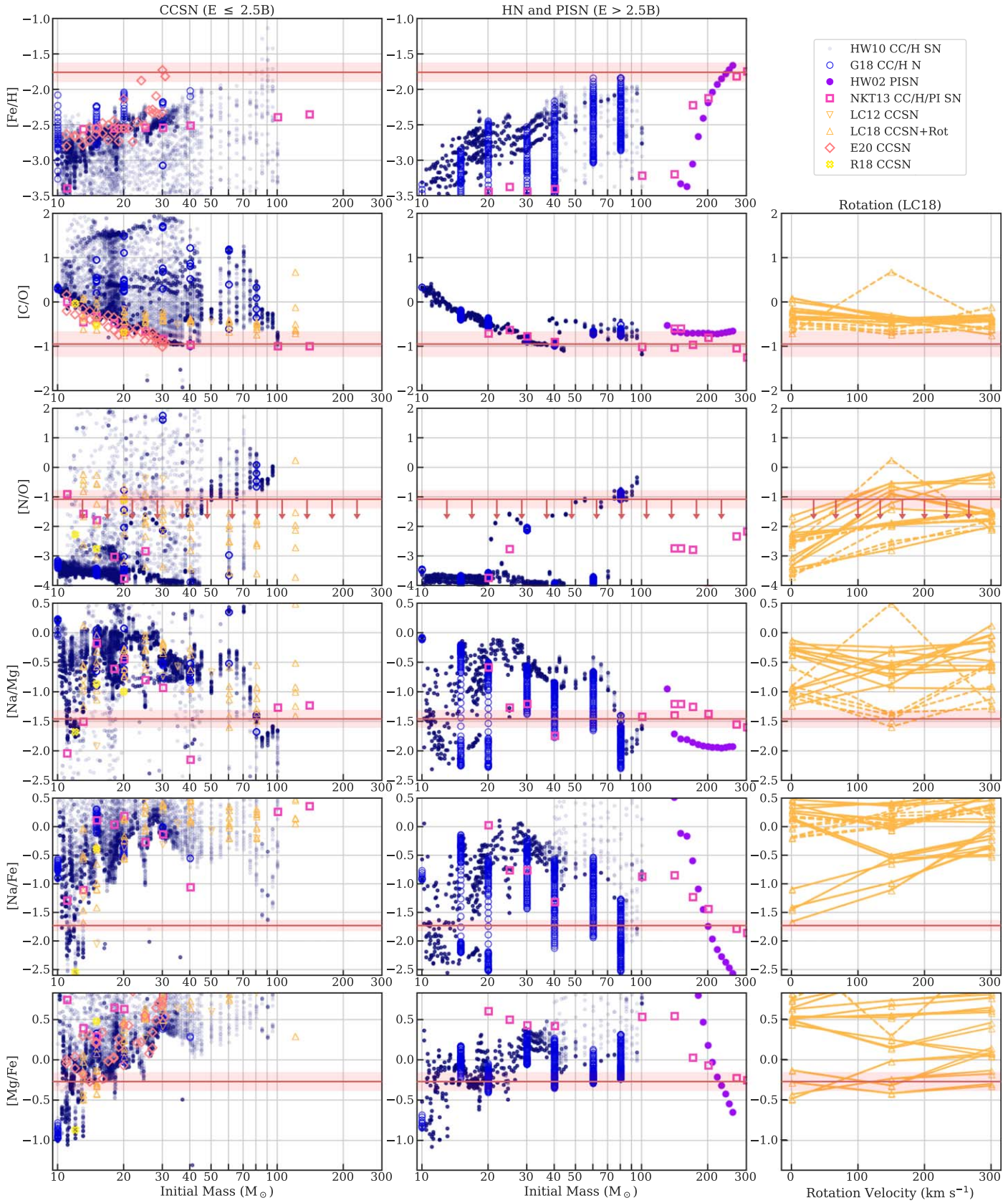

Figure 9. Light element ratios vs. initial mass for CCSNe (left column; HW10, G18, NKT13, LC12, LC18, E20, R18), HNe and PISNe (center column; HW10, G18, NKT13, HW02), and rotation velocity (right column; LC18 only). N and Na are not plotted for E20. In the right column, the same mass and metallicity at different rotation velocities are connected by solid lines ($< 50\,M_{\odot}$) or dashed lines ($\geqslant 50\,M_{\odot}$). These figures explain the first rows of Table 2.

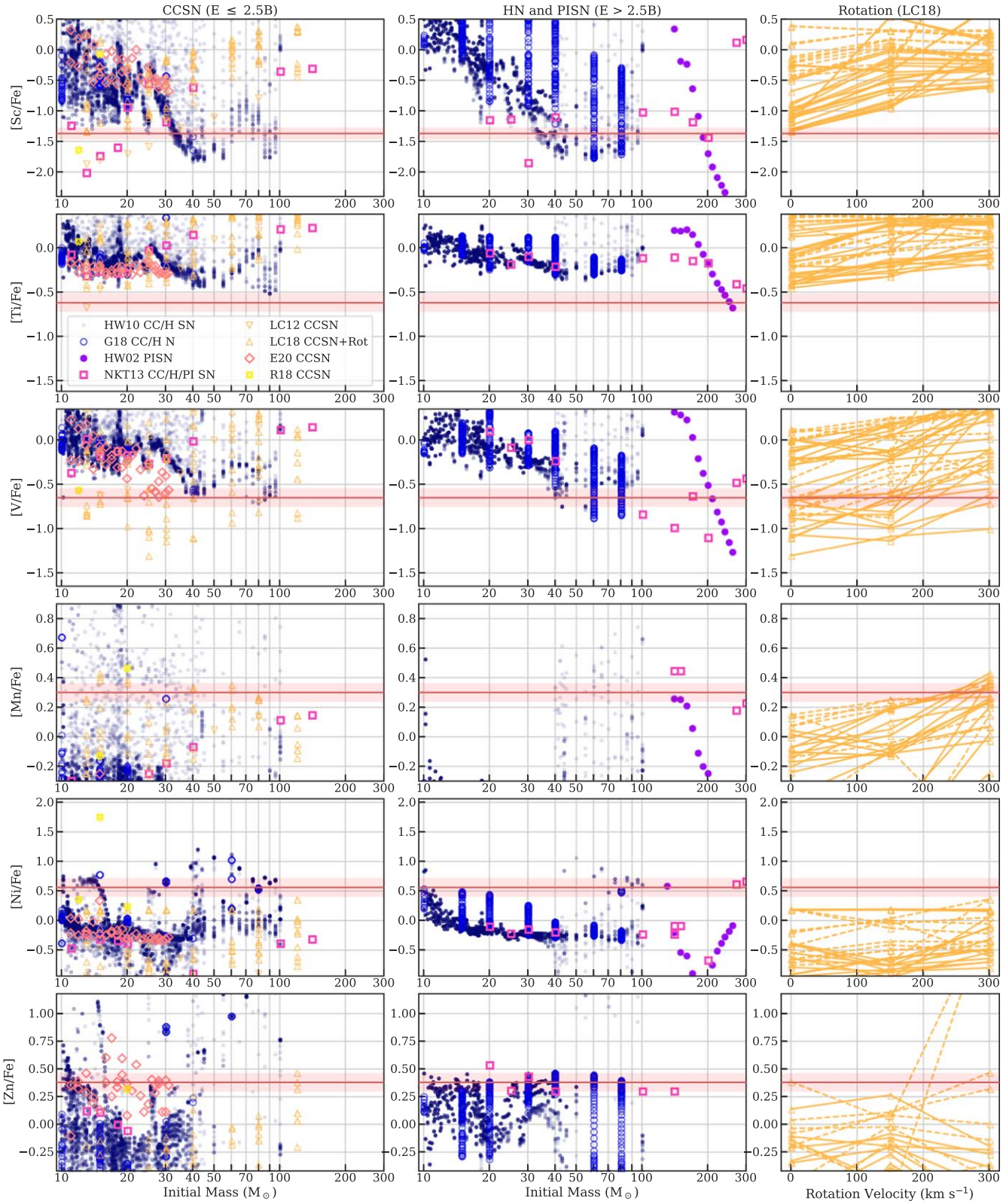

Figure 10. Iron-peak element ratios vs. initial mass for CCSNe (left column; HW10, G18, NKT13, LC12, LC18, E20, R18), HNe and PISNe (center column; HW10, G18, NKT13, HW02), and rotation velocity (right column; LC18 only). In the right column, the same mass and metallicity at different rotation velocities are connected by solid lines ($< 50\,M_{\odot}$) or dashed lines ($\geqslant 50\,M_{\odot}$). These figures explain the middle rows of Table 2.

process in fast-rotating massive stars would increase Ba substantially (Chiappini 2013; Choplin et al. 2018).

We see that Fe-peak synthesis is very uncertain in both CCSNe and HNe, reflecting uncertainties in the explosion mechanism. The lighter Fe-peak elements (Sc, V) tend to prefer higher-mass CCSNe or HNe, and almost no CCSN or HN models can explain the low [Ti/Fe]. The high Mn is problematic; for CCSNe and HNe, it can only be matched

Table 2
Death Matrix

Criterion	CCSN			HN			PISN		Add Rapid
Mass ($M_\odot$)	<20	20–50	50–100	<20	20–50	50–100	140–200	200–260	Rotation
High [Fe/H] ~ -1.8	×	×?	×?	×	×	×?	×	✓	…
Low [C/O] ~ -1.0	×	✓?	✓?	×	✓	✓	✓	✓	No change
Low [N/O] < -1.0	✓?	✓?	×?	✓	✓	✓?	✓	✓	Increases up to 100×
Low [Na/Mg] ~ -1.5	✓?	×	✓?	✓?	✓?	✓	✓	✓?	Varying predictions
Low [Mg/Fe] ~ -0.3	✓	×	×	✓	✓?	✓?	×	✓	Little change
Low [Sc,Ti,V/Fe] < -0.5	×?	✓?	✓?	×	✓?	✓?	×	✓	Increases by 2–10×
High [Mn/Fe] ~0.3	×?	×?	×?	×?	×?	×?	✓?	×	Increases by 2–3×
High [Ni,Zn/Fe] ~0.5	✓?	×?	×?	✓?	✓?	✓?	×	×	Little change
High [Sr–Pd/Fe] >0.5	✓?	✓?	✓?	✓?	✓?	✓?	×	×	Increases all
Low [Ba/Fe] ~ -2.8	✓	✓	✓	✓	✓	✓	✓	✓	Increases Ba
Explosion expected	✓	✓?	×	✓	✓?	✓?	✓	✓	Helps explodability

Note.
[a] The ✓ and × signify whether nearly all models in a particular category are found to match or fail to match a given criterion. The ✓? denotes that most models in a category satisfy the criterion, but there are large uncertainties and/or important exceptions. Similarly, the ×? denotes that most models do not satisfy the criterion, but there are large uncertainties and/or large variations in predictions. All Fe-peak predictions for CCSNe and HNe have significant uncertainties. The last row indicates whether an explosion is theoretically expected in this mass range for metal-poor progenitors.

Table 3
Nucleosynthesis Yield Grids

Key	Explosion	Mass Range ($M_\odot$)	Energy (B)	Metallicity (Solar)	Comments/Other Parameters
HW10 CC	Piston (S4)	10–100	0.3–2.4	0	Mixing: none to 0.251
HW10 HN	Piston (S4)	10–100	3, 5, 10	0	Mixing: none to 0.251
G18 CC	Piston (S4)	10–80	0.1–2.0	0	Mixing: none to 0.251
G18 HN	Piston (S4)	10–80	2.5–200	0	Mixing: none for $E > 5$ B
HW02	PISN	140–260	9–87	0	Initial mass from He core mass Energy calculated self-consistently
NKT13 CC	Thermal bomb	11–140	1	0	Mixing and fallback
NKT13 HN	Thermal bomb	20–140	10–71	0	Mixing and fallback
NKT13 PI	PISN	140–300	16–50	0	Energy calculated self-consistently
LC12	Kinetic bomb	13–80	N/A	0	…
LC18	Kinetic bomb	13–120	N/A	$10^{-3,\ -2}$	Rotation: 0, 150, 300 km s^{-1} Includes all forced explosion models
E20	Engine-driven	11–31	0.3–1.7	0, 10^{-4}	Energy calculated self-consistently
R18	Shock and cool	12–25	N/A	$10^{-2.3}$	Delayed explosions

Note.
[a] Restricted to metallicities [Z/H]< -1.5. Other models not searched are NKT13 $Z/Z_\odot = 10^{-1.3,-0.7,-0.4,0,+0.4}$, LC18 $Z/Z_\odot = 0.1$, 1, and R18 $Z/Z_\odot = 10^{-1.3,-0.5,-0.2,0}$.

by lower-mass, higher-metallicity progenitors with rapid rotation or fine-tuned mixing/fallback (which would not produce high [Fe/H] ratios). However, those same LC18 models also greatly overpredict the Sc, Ti, and V abundances. The low-mass PISNe also produce the appropriate [Mn/Fe], but only because they produce so little Fe. Higher explosion energies ($E > 10$ B) can produce high [Zn/Fe] ratios, but Ni is difficult overall except in lower-mass CCSNe.

B.2. Search through Single Star Nucleosynthesis Yields

We performed an extensive search of supernova yield grids covering a wide range of possible nucleosynthesis sites, covering elements from C to Zn: primordial CCSNe exploded with a piston (Heger & Woosley 2010; assuming the S4 location), thermal bomb (Nomoto et al. 2013), and kinetic bomb (Limongi & Chieffi 2012) with various assumptions for mixing and fallback; CCSNe of higher metallicities (Nomoto et al. 2013; Ritter et al. 2018) with rotation (Limongi & Chieffi 2018) and engine-driven explosions (Ebinger et al. 2020); HNe of varying energies (Nomoto et al. 2013; Grimmett et al. 2018); and primordial PISNe (Heger & Woosley 2002; Nomoto et al. 2013). We also examined CCSNe of solar metallicity binary stripped stars (Farmer et al. 2023) and thermonuclear Type Ia supernovae (references in Reggiani et al. 2023), though none of these were good fits, so we do not discuss them further. We only included models with [Z/H] < -1.5, except for the binary stripped star supernovae, where only solar metallicity models exist. We also qualitatively considered how abundance patterns would be affected by nucleosynthesis of jets interacting with stellar envelopes (Grimmett et al. 2021) and rotation (Ekström et al. 2008; Frischknecht et al. 2016), as these references did not provide full yield tables of all elements. A summary of the searched models is given in Table 3.

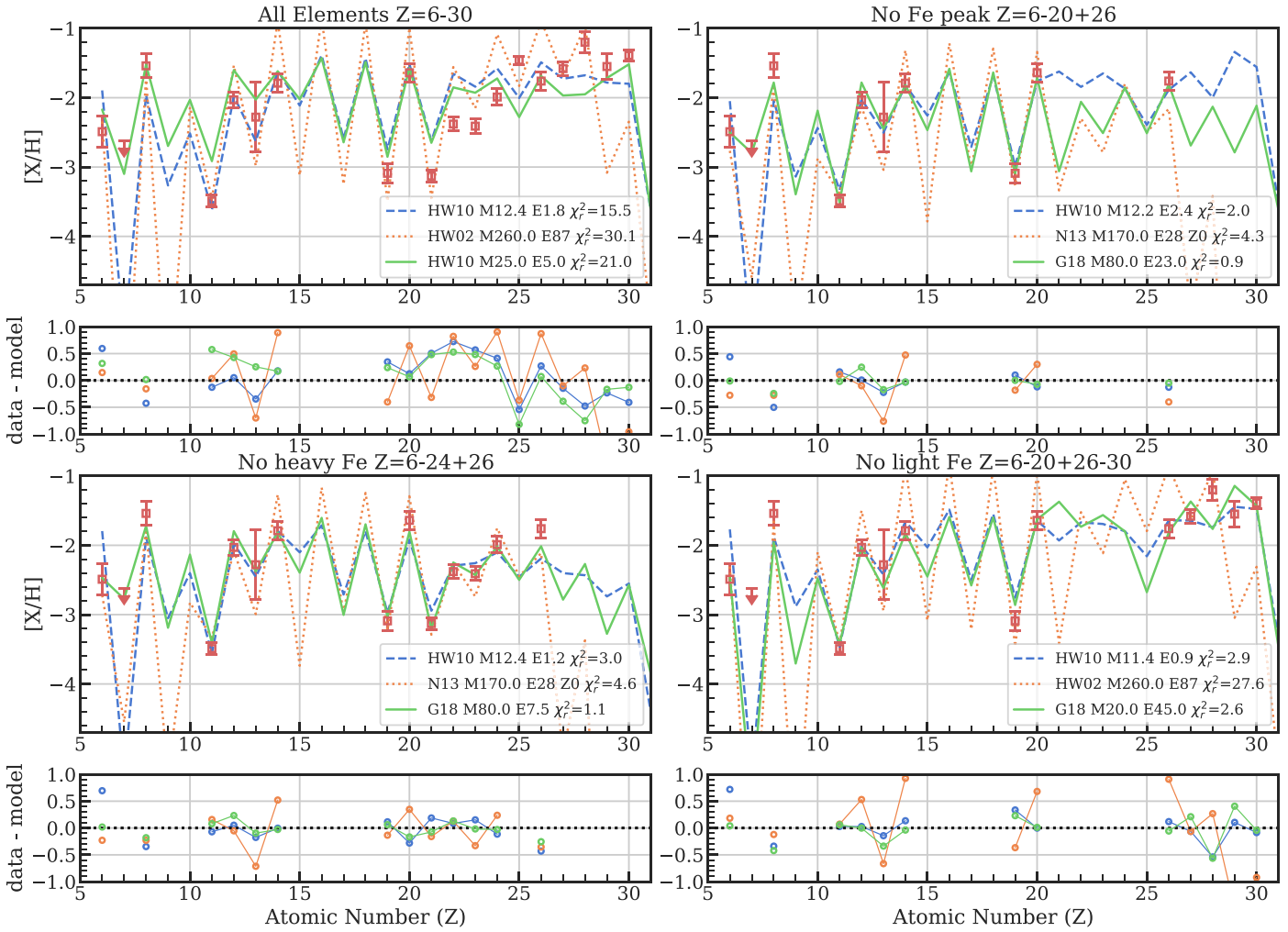

Figure 11. Results of grid search through CCSN, PISN, and HN models for different permutations of elements. The best-fit model is shown in the legend: dashed blue = CCSN, dotted orange = PISN, solid green = HN. Reduced χ^2 is shown in the legend. See text for details.

To investigate the yield grids, we used two search algorithms: `Starfit`, which does χ^2 minimization (Heger & Woosley 2010), and a code based on Ji et al. (2020b) that minimizes the mean absolute deviation (MAD; normalized by abundance uncertainty), which is more robust to outliers. In both searches, the gas dilution is a free parameter; i.e., we allow the abundance pattern of each model to shift arbitrarily up and down in log space, ignoring the total metallicity constraint that would rule out essentially all models. The two different search strategies resulted in the same overall conclusions.

No model or site was found to adequately reproduce the entire observed abundance pattern, so the best-fit models depended heavily on the choice of elements to fit. After examining many permutations, it became clear that the lighter elements with $Z \leqslant 20$ could generally be fit by many types of supernovae, but the iron peak was never well fit. We thus present the best-fit CCSN, HN, and PISN models for four permutations of elements in Figure 11:

(1) including all elements from Z = 6–30,
(2) fitting elements from Z = 6–24 and 26 to exclude the enhancements in heavier Fe-peak elements as well as the difficult element Mn,
(3) fitting elements from Z = 6–20 and 26–30 to remove the deficiency of lighter Fe-peak elements, and
(4) fitting Z = 6–20 and 26 to remove all Fe-peak elements other than iron.

When fitting all elements from C to Zn (top left panel), the best fits were achieved by a low-mass (12.4 $M_\odot$) primordial supernova from Heger & Woosley (2010), but with a reduced χ^2 of 15.5 that indicates a terrible fit. This model is able to explain elements from Na–Si and Ca, but it fails C and O and the entire Fe peak. Other CCSN models have similar issues. If we remove all Fe-peak elements other than Fe (top right panel), we see that there is no CCSN or PISN able to reproduce all the light elements. Low-mass CCSNe fail due to C/O as shown, while high-mass ordinary-energy CCSNe produce too little Fe. The moderate-sized odd–even effect in J0931 + 0038 suggests lower-mass PISNe, but these produce insufficient Fe. However, a massive (80 $M_\odot$) high-energy (23 B) HN from Grimmett et al. (2018) is able get a near-perfect fit to the light elements while producing enough iron (χ^2_r = 0.9). This scenario does not change much if we add back in Sc, Ti, V, and Cr (bottom left panel), where the CCSN and PISN continue to have issues but the 80 $M_\odot$ HN still works well (χ^2_r = 1.1). However, if we instead exclude the light Fe peak and add back the heavy Fe peak (bottom right), again, no model gives a satisfactory fit.

This exploration suggests that if a single star is to produce the abundance pattern, the best candidate is an 80 $M_\odot$ HN.

This can explain all the light elements from C to Cr, and the exact Fe peak can be adjusted based on the energy. Plausibly, fixes to the heavy Fe-peak pattern and enhanced Mn could come from nucleosynthesis in jets and/or be induced by rotation or other 3D effects, which are not extensively explored in existing model grids. However, current nucleosynthesis models suggest this does not work, as jets tend to coproduce Sc/Ti/V and Co–Zn (Tominaga 2009; Grimmett et al. 2021). Additionally, all these higher-energy HN models violate the metallicity constraint (Section 4.1). One other option is adding *i*-process to PISNe, which could resolve some of the problems with those models (see Appendix B.4).

B.3. Combining Two Sites

As no individual site provided a satisfactory fit to the entire abundance pattern from C to Zn ($Z = 6 - 30$), we next ran joint fits between all possible pairs of sites. Note that combining two sites is not a plausible explanation for J0931 + 0038 (see Section 4.1), but this exploration can identify physical conditions in existing calculations that could explain parts of the abundance pattern if combined into one site. It is expensive to consider all pairs, and there is no analytic solution allowing arbitrary dilution, so we approximated the solution by first fitting each yield to the star individually following Ji et al. (2020b), then performing a brute-force optimization of the minimum absolute deviation (normalized by abundance error) by allowing the dilution of each yield to drift by −3.0 to +1.0 dex in units of 0.1 dex from the initial fit. For simplicity, we ignored the N upper limit.

For this exercise, we split our yield tables into CCSNe (CC), HNe, PISNe (PI), and Type Ia supernovae (IA). The Heger & Woosley (2010) and Grimmett et al. (2018) yield tables spanned a large range of energies, so we somewhat arbitrarily split them into CCSNe and HNe at $E = 2.5$ B. We also created an empirical ISM model using abundances from SAGA (Suda et al. 2008), fitting third-order polynomials to [Fe/H] versus [X/H] as shown in Figure 8 and assuming [X/Fe] = 0 for elements not in that figure. We created ISM compositions at [Fe/H] = −3.5 to −1.5 in steps of 0.5 dex and included them as a separate yield table in our fits.

The results are shown in Figures 12 and 13. Figure 12 shows a search for the optimal combination of CC+CC, HN+HN, and PI+PI (top row) and crossing supernova types CC+HN, CC+PI, and HN+PI (bottom row). Figure 13 crosses each supernova type with Type Ia (top row) and ISM (bottom row). These specific fits were chosen to have the smallest possible minimum absolute deviation of all combinations. Close ties were broken by choosing models that illustrate specific physics.

The immediate overall conclusion is that no pairs of models can fit the entire abundance pattern, despite the vastly expanded model space compared to single site fits. The reduced χ^2 and MAD should be near 1 for reasonable fits, and the lowest MAD is 1.9. There is enough freedom that the light elements with $Z \leqslant 20$ are generally fit well. However, the Fe peak from $Z = 21$ to 30 has many issues, especially for Sc ($Z = 21$), Mn ($Z = 25$), and the overall enhanced Co–Zn ($Z = 27$–30). Fitting all three of these simultaneously is not possible even after searching through over 20,000 yield sets.

Two models show up repeatedly in these fits as being able to solve some of the Fe-peak problems. First, in the top row of Figure 13, off-center deflagration explosions of Chandrasekhar-mass white dwarfs (here showing yields from Fink et al. 2014) are able to achieve a high [Mn/Fe] and [Ni/Fe] ratio that broadly matches J0931 + 0038, though no Type Ia supernova is able to produce similarly high levels of Zn. Though white dwarfs are likely not relevant progenitors for nucleosynthesis in J0931 + 0038 (see Section 4.1), the high neutron fractions achieved in those white dwarfs could potentially be achieved in massive stars, although there is tension with the low neutron fractions needed to have a large odd–even effect. Second, the 15 $M_\odot$ CC model from Ritter et al. (2018) shows up several times in both figures because it is able to produce large amounts of Co–Zn. This model ejects a large amount of material near the mass cut that was in nuclear statistical equilibrium (NSE), resulting in a very strong alpha-rich freeze-out that produces this pattern, as well as some heavier elements all the way up to Mo ($Z = 42$; see Figure 28 of Ritter et al. 2018; Woosley & Hoffman 1992). Ejecting substantial amounts of this NSE material is a promising future path to reproducing the abundance pattern of J0931 + 0038. One example of this could be late-time mass loss induced by close binary interactions. The lighter elements (C–Ca) could be hydrostatically synthesized by a 80 $M_\odot$ progenitor to match J0931 + 0038, but late mass loss from binary stripping after the CO core mass is set could push the mass cut closer to the center of the star. Note that Case C mass transfer (after igniting central He burning) is a typical outcome of massive metal-poor star binary evolution (de Mink et al. 2008).

Finally, the models including ISM did not work well. As expected, the ISM in the PISN+ISM was able to fix the overly strong odd–even effect in the light elements for the 260 $M_\odot$ PISN, but it could not contribute to the problems with the Fe peak. Though we allowed the ISM to be metallicities from [Fe/H] = −3.5 to −1.5, the −3.5 ISM always came to the forefront primarily because it helped most models fit the [C/O] ratio better while also filling in any missing amount of Na, K, or Sc. It is worth noting that the [C/O] ratio in our ISM model is likely too low, since it is only possible to detect O in the data when it is highly enhanced (and similar for N).

B.4. Full Fits from Z = 6 to 56 Including Neutron-capture Elements

There are few models that self-consistently predict nucleosynthesis yields of both lighter and heavier elements. We thus constructed plausible combinations of our best-fit explosion models (HN and PISN) and heavy-element nucleosynthesis patterns (computed through simulation-based or parameterized trajectories), combining them using the two-component search from `Starfit` (Heger & Woosley 2010). Our goal was to create realistic abundance patterns for scenarios that could simultaneously explain both the light and heavy elements in J0931 + 0038. These results were used to create the models including neutron-capture elements in Figure 5. A PISN combined with an *i*-process emerges as one possible explanation for simultaneously producing the observed abundance pattern and high metallicity of J0931 + 0038, although no such theoretical models currently exist in the literature. An HN combined with an *r*/*i*-process or a neutrino-driven wind (if such an explosion occurs) may also provide a good match to the observed abundances. In this section, we elaborate on general considerations for heavy-element nucleosynthesis, followed by discussion of which combinations are realistic.

Considering the heavy elements in J0931 + 0038 ($Z > 35$), the enhancement in Sr all the way out to Pd, combined with

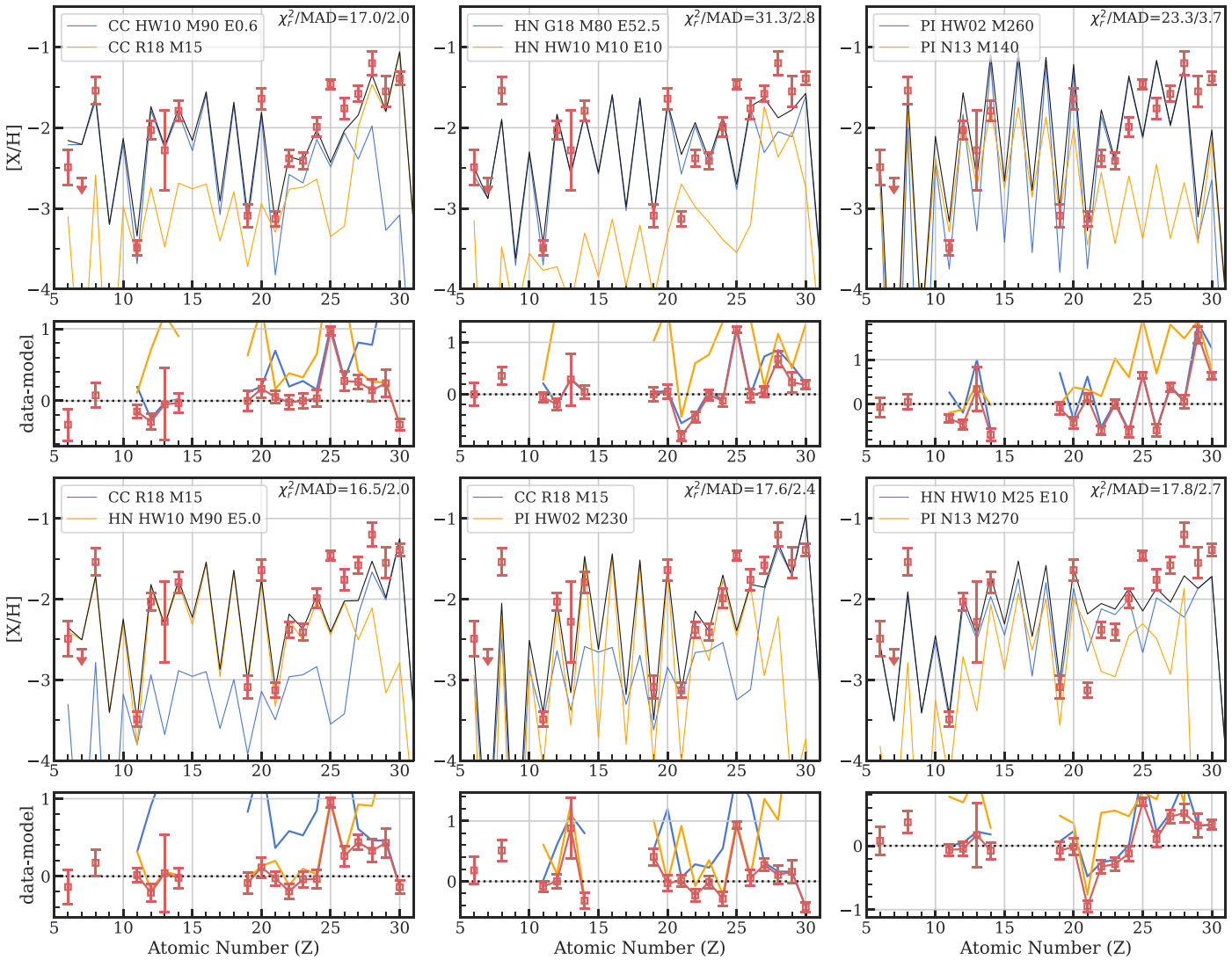

Figure 12. Best-fit results of fitting abundances of J0931 + 0038 (red points) combining CCSNe, HNe, and PISNe with each other. The large panels shows the fits in [X/H], while the smaller panels indicate the residual (data–model). The blue and orange lines indicate two different models described in the top left legend of each panel, and the black line indicates their sum. The top right corner of the large panels shows reduced chi-squares and the error-normalized MAD. References: E20, G18, HW02, HW10, N13, R18. See Section B.3 for discussion.

low Ba and Eu, provides a strong constraint on the conditions needed for their synthesis. There will be insignificant contributions from the main *r*-process that synthesizes a relatively large amount of Ba and Eu (e.g., Holmbeck et al. 2023) and the main *s*-process that synthesizes a large amount of Ba relative to Sr in metal-poor stars (e.g., Lugaro et al. 2012). The *i*-process generally has a similar challenge as the *s*-process of over-producing Ba (e.g., Hampel et al. 2016; Côté et al. 2018). This is mostly driven by the assumption of solar-scaled initial abundances for stellar simulations at low metallicity, where an early increase of the Ba production is mostly fed from seed abundances in the Sr–Zr region. The *i*-process production at the first neutron-magic peak of Rb–Zr is instead due to neutron captures on the Fe seeds (e.g., Herwig et al. 2011), and it does not depend on their initial abundances. Finally, most ν-driven wind models only produce significant amounts of elements up to Mo but are unable to extend out to Pd (Fröhlich et al. 2006; Wanajo 2006; Wanajo et al. 2018).

From published model grids, we find that a weak *r*-process with $Y_e \sim 0.25$ and entropy of $12k_B$ per baryon (or something slightly more neutron-poor) allows the synthesis of the first-peak elements without producing a substantial amount of Ba (e.g., Nishimura et al. 2017; Holmbeck et al. 2023). The detailed pattern of any individual Y_e trajectory does not match our observations, but a mixture of ejecta conditions is expected and can likely be combined to reproduce the detailed pattern (e.g., Farouqi et al. 2010; Holmbeck et al. 2019). We also find that a high-entropy (120 k_B per nucleon) and proton-rich ($Y_e = 0.54$) neutrino-driven wind trajectory is able to match the light elements out to Pd, although it is not clear if such conditions can be achieved in actual supernovae (Bliss et al. 2018).

In Section 4, we discussed a computational experiment for *i*-process nucleosynthesis where we reduced abundances of elements heavier than Fe. This is justified, as metal-poor gas is deficient in the neutron-capture elements compared to iron (see Figure 8 and Cescutti et al. 2013). Our *i*-process models thus use the nucleosynthesis framework from Bertolli et al. (2013) and Roederer et al. (2016, 2022) but reduce the initial heavy-element abundances with respect to Fe by 10 times (e.g., [Sr/Fe] = −1 and [Ba/Fe] = −1). With this change, it is

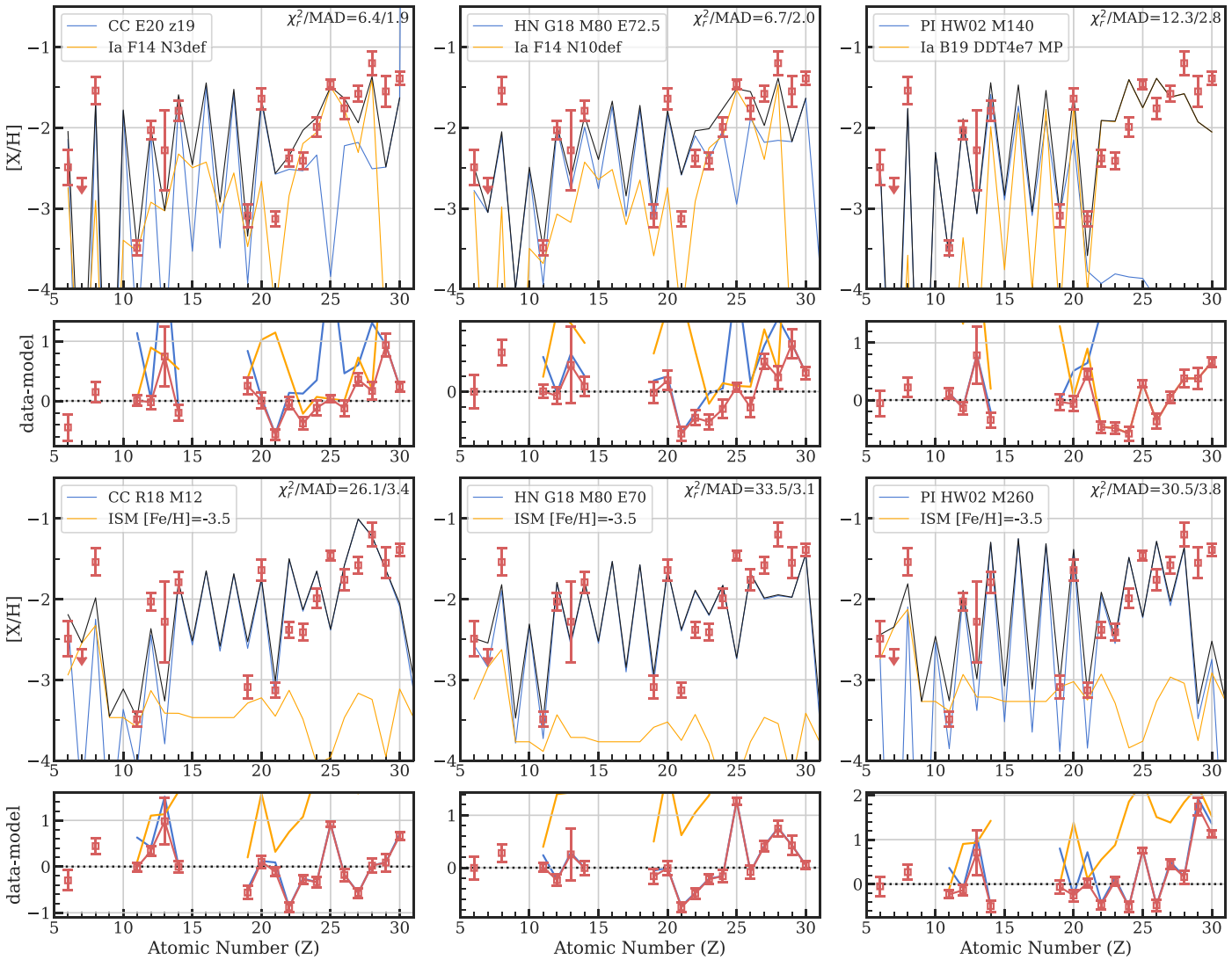

Figure 13. Best-fit results of fitting abundances of J0931 + 0038 (red points) combining CCSNe, HNe, and PISNe with Type Ia and ISM. Same lines as Figure 12. References: Bravo et al. (2019, B19), E20, Fink et al. (2014, F14), G18, HW10, R18. See Section B.3 for discussion.

possible to satisfy the low Ba constraint and at the same time obtain an efficient production in the Rb–Ru mass region as observed in J0931 + 0038. However, while the *i*-process produces heavy elements, the abundances of intermediate-mass elements (in particular the less abundant odd elements) can also be affected. An example is the observed enhancement of Sc with respect to Ca in the post-AGB star Sakurai's object, where Sc is coproduced with heavy elements in the Rb–Zr region (Herwig et al. 2011). Another example is extra production of Na and Al (e.g., Clarkson et al. 2018).

We now discuss whether the production of heavy elements through the channels described above is a realistic possibility in CCSN, HN, and PISN explosions. CCSNe/HNe are thought to be accompanied by heavy-element production in neutrino-driven winds from a neutron star remnant, either through a weak *r*-process or under proton-rich conditions, although the detailed properties of these winds are being investigated (Fröhlich et al. 2006; Pruet et al. 2006; Arcones & Montes 2011; Arcones & Thielemann 2013; Wanajo 2013; Fujibayashi et al. 2015). A weak *r*-process with $Y_e \lesssim 0.25$ could potentially occur in accretion disk winds around a black hole (e.g., Pruet et al. 2004; Surman et al. 2006). Altogether, the production of enhanced light neutron-capture elements out to Pd in such winds suggests scenarios involving material ejected from a neutron star or black hole accretion disk. These remnants are a natural and expected outcome of CCSN/HN explosions, lending support to the scenarios where an HN is combined with a weak *r*-process or proton-rich neutrino-driven wind. On the other hand, PISNe leave no remnant behind and hence cannot produce neutron-capture elements through these channels.

The other possibility for producing heavy elements, the intermediate (*i*) neutron-capture process, is a recently revived process of interest (e.g., Hampel et al. 2016; Roederer et al. 2016; Côté et al. 2018). The source of the *i*-process in massive metal-poor stars is proton ingestion due to mixing with convective He shells (Cowan & Rose 1977; Banerjee et al. 2018; Clarkson et al. 2018). However, it is not yet clear if 3D simulations including convection are able to trigger the proton ingestion that would induce the *i*-process (Herwig et al. 2014; Woodward et al. 2015). Nonetheless, this possibility lends support to the scenario where an HN combined with an *i*-process could explain the abundances in J0931 + 0038.

If massive metal-poor progenitors of CCSNe or HNe can be affected by proton ingestion events that activate the *i*-process,

we can expect that the same may happen for PISN progenitors. If this occurs, the *i*-process in a PISN progenitor could not only produce the neutron-capture elements, but it might also help fill in the low abundances of light odd elements, while also increasing the abundance of Zn that otherwise rules out PISN models. However, there are no PISN models available yet taking into account the impact of such events within their integrated yields. Future generations of PISN models including proton ingestion and the supernova explosion will be paramount to explore this scenario in greater detail.

ORCID iDs

Alexander P. Ji https://orcid.org/0000-0002-4863-8842
Sanjana Curtis https://orcid.org/0000-0002-3211-303X
Nicholas Storm https://orcid.org/0000-0002-5259-3974
Vedant Chandra https://orcid.org/0000-0002-0572-8012
Kevin C. Schlaufman https://orcid.org/0000-0001-5761-6779
Keivan G. Stassun https://orcid.org/0000-0002-3481-9052
Alexander Heger https://orcid.org/0000-0002-3684-1325
Marco Pignatari https://orcid.org/0000-0002-9048-6010
Adrian M. Price-Whelan https://orcid.org/0000-0003-0872-7098
Maria Bergemann https://orcid.org/0000-0002-9908-5571
Guy S. Stringfellow https://orcid.org/0000-0003-1479-3059
Carla Fröhlich https://orcid.org/0000-0003-0191-2477
Henrique Reggiani https://orcid.org/0000-0001-6533-6179
Erika M. Holmbeck https://orcid.org/0000-0002-5463-6800
Jamie Tayar https://orcid.org/0000-0002-4818-7885
Shivani P. Shah https://orcid.org/0000-0002-3367-2394
Emily J. Griffith https://orcid.org/0000-0001-9345-9977
Chervin F. P. Laporte https://orcid.org/0000-0003-3922-7336
Andrew R. Casey https://orcid.org/0000-0003-0174-0564
Keith Hawkins https://orcid.org/0000-0002-1423-2174
Danny Horta https://orcid.org/0000-0003-1856-2151
William Cerny https://orcid.org/0000-0003-1697-7062
Pierre Thibodeaux https://orcid.org/0000-0002-3867-3927
Sam A. Usman https://orcid.org/0000-0003-0918-7185
João A. S. Amarante https://orcid.org/0000-0002-7662-5475
Rachael L. Beaton https://orcid.org/0000-0002-1691-8217
Phillip A. Cargile https://orcid.org/0000-0002-1617-8917
Cristina Chiappini https://orcid.org/0000-0003-1269-7282
Charlie Conroy https://orcid.org/0000-0002-1590-8551
Jennifer A. Johnson https://orcid.org/0000-0001-7258-1834
Juna A. Kollmeier https://orcid.org/0000-0001-9852-1610
Haining Li https://orcid.org/0000-0002-0389-9264
Sarah Loebman https://orcid.org/0000-0003-3217-5967
Georges Meynet https://orcid.org/0000-0001-6181-1323
Dmitry Bizyaev https://orcid.org/0000-0002-3601-133X
Joel R. Brownstein https://orcid.org/0000-0002-8725-1069
Pramod Gupta https://orcid.org/0000-0002-3956-2102
Sean Morrison https://orcid.org/0000-0002-6770-2627
Kaike Pan https://orcid.org/0000-0002-2835-2556
Hans-Walter Rix https://orcid.org/0000-0003-4996-9069
José Sánchez-Gallego https://orcid.org/0000-0003-2486-3858

References

Abbott, R., Abbott, T. D., Acernese, F., et al. 2023, PhRvX, 13, 011048
Abdurro'uf, Accetta, K., Aerts, C., et al. 2022, ApJS, 259, 35
Abohalima, A., & Frebel, A. 2018, ApJS, 238, 36
Aguado, D. S., Allende Prieto, C., González Hernández, J. I., et al. 2016, A&A, 593, A10
Almeida, A., Anderson, S. F., Argudo-Fernández, M., et al. 2023, ApJS, 267, 44
Amarante, J. A. S., Debattista, V. P., Beraldo e Silva, L., Laporte, C. F. P., & Deg, N. 2022, ApJ, 937, 12
Andrievsky, S., Bonifacio, P., Caffau, E., et al. 2018, MNRAS, 473, 3377
Arcones, A., & Montes, F. 2011, ApJ, 731, 5
Arcones, A., & Thielemann, F. K. 2013, JPhG, 40, 013201
Arenou, F., Luri, X., Babusiaux, C., et al. 2018, A&A, 616, A17
Asplund, M., Grevesse, N., Sauval, A. J., & Scott, P. 2009, ARA&A, 47, 481
Astropy Collaboration, Robitaille, T. P., Tollerud, E. J., et al. 2013, A&A, 558, A33
Audouze, J., & Silk, J. 1995, ApJL, 451, L49
Avallone, E. A., Tayar, J. N., van Saders, J. L., et al. 2022, ApJ, 930, 7
Bailer-Jones, C. A. L., Rybizki, J., Fouesneau, M., Demleitner, M., & Andrae, R. 2021, AJ, 161, 147
Banerjee, P., Qian, Y.-Z., & Heger, A. 2018, ApJ, 865, 120
Beers, T. C., Preston, G. W., & Shectman, S. A. 1992, AJ, 103, 1987
Belokurov, V., Erkal, D., Evans, N. W., Koposov, S. E., & Deason, A. J. 2018, MNRAS, 478, 611
Bergemann, M. 2011, MNRAS, 413, 2184
Bergemann, M., Collet, R., Amarsi, A. M., et al. 2017, ApJ, 847, 15
Bergemann, M., Gallagher, A. J., Eitner, P., et al. 2019, A&A, 631, A80
Bergemann, M., Hansen, C. J., Bautista, M., & Ruchti, G. 2012a, A&A, 546, A90
Bergemann, M., Lind, K., Collet, R., Magic, Z., & Asplund, M. 2012b, MNRAS, 427, 27
Bergemann, M., Hoppe, R., Semenova, E., et al. 2021, MNRAS, 508, 2236
Bergemann, M., Kudritzki, R.-P., Würl, M., et al. 2013, ApJ, 764, 115
Bergemann, M., & Nordlander, T. 2014, in Determination of Atmospheric Parameters, ed. E. Ewa, B. Smalley, & W. Pych (Berlin: Springer), 169
Bergemann, M., Pickering, J. C., & Gehren, T. 2010, MNRAS, 401, 1334
Bernstein, R., Shectman, S. A., Gunnels, S. M., Mochnacki, S., & Athey, A. E. 2003, Proc. SPIE, 4841, 1694
Bertolli, M. G., Herwig, F., Pignatari, M., & Kawano, T. 2013, arXiv:1310.4578
Bianchi, L., Shiao, B., & Thilker, D. 2017, ApJS, 230, 24
Bliss, J., Arcones, A., & Qian, Y. Z. 2018, ApJ, 866, 105
Boccioli, L., Roberti, L., Limongi, M., Mathews, G. J., & Chieffi, A. 2023, ApJ, 949, 17
Bolton, A. S., Schlegel, D. J., Aubourg, É., et al. 2012, AJ, 144, 144
Brasseur, C. E., Phillip, C., Fleming, S. W., Mullally, S. E., & White, R. L., 2019, Astrocut: Tools for creating cutouts of TESS images, Astrophysics Source Code Library, ascl:1905.007
Brauer, K., Andales, H. D., Ji, A. P., et al. 2022, ApJ, 937, 14
Bravo, E., Badenes, C., & Martínez-Rodríguez, H. 2019, MNRAS, 482, 4346
Bromm, V. 2013, RPPh, 76, 112901
Brown, A. G., Vallenari, A., Prusti, T., et al. 2021, A&A, 649, A1
Burrows, A., & Vartanyan, D. 2021, Natur, 589, 29
Burrows, A., Vartanyan, D., Dolence, J. C., Skinner, M. A., & Radice, D. 2018, SSRv, 214, 33
Caffau, E., Bonifacio, P., Sbordone, L., et al. 2013, A&A, 560, A71
Cargile, P. A., Conroy, C., Johnson, B. D., et al. 2020, ApJ, 900, 28
Carlin, J. L., Sheffield, A. A., Cunha, K., & Smith, V. V. 2018, ApJL, 859, L10
Casey, A. R. 2014, PhD Thesis, Australian National Univ.
Casey, A. R., & Schlaufman, K. C. 2015, ApJ, 809, 110
Castelli, F., & Kurucz, R. L. 2003, in IAU Symp. 210, Modelling of Stellar Atmospheres, Poster Contributions, ed. N. Piskunov, W. W. Weiss, & D. F. Gray (San Francisco, CA: ASP), A20
Cayrel, R., Depagne, E., Spite, M., et al. 2004, A&A, 416, 1117
Cescutti, G., Chiappini, C., Hirschi, R., Meynet, G., & Frischknecht, U. 2013, A&A, 553, A51
Chambers, K. C., Magnier, E. A., Metcalfe, N., et al. 2016, arXiv:1612.05560
Chance, Q., Foreman-Mackey, D., Ballard, S., et al. 2022, arXiv:2206.11275
Chen, K.-J., Heger, A., Woosley, S., et al. 2014, ApJ, 790, 162
Chiappini, C. 2013, AN, 334, 595
Choi, J., Dotter, A., Conroy, C., et al. 2016, ApJ, 823, 102
Choplin, A., Hirschi, R., Meynet, G., et al. 2018, A&A, 618, A133
Cioffi, D. F., McKee, C. F., & Bertschinger, E. 1988, ApJ, 334, 252
Clarkson, O., Herwig, F., & Pignatari, M. 2018, MNRAS, 474, L37
Conroy, C., Bonaca, A., Cargile, P., et al. 2019, ApJ, 883, 107
Côté, B., Denissenkov, P., Herwig, F., et al. 2018, ApJ, 854, 105
Cowan, J. J., & Rose, W. K. 1977, ApJ, 212, 149
Cowan, J. J., Sneden, C., Burles, S., et al. 2002, ApJ, 572, 861
Curtis, S., Ebinger, K., Fröhlich, C., et al. 2019, ApJ, 870, 2
Da Costa, G. S., Bessell, M. S., Mackey, A. D., et al. 2019, MNRAS, 489, 5900

Dawson, K. S., Schlegel, D. J., Ahn, C. P., et al. 2013, AJ, 145, 10
de Mink, S. E., Pols, O. R., & Yoon, S. C. 2008, in AIP Conf. Ser. 990, First Stars III, ed. B. W. O'Shea & A. Heger (Melville, NY: AIP), 230
deBoer, R. J., Görres, J., Wiescher, M., et al. 2017, RvMP, 89, 035007
Doherty, C. L., Gil-Pons, P., Siess, L., & Lattanzio, J. C. 2017, PASA, 34, e056
Doi, M., Tanaka, M., Fukugita, M., et al. 2010, AJ, 139, 1628
Dotter, A. 2016, ApJS, 222, 8
Ebinger, K., Curtis, S., Ghosh, S., et al. 2020, ApJ, 888, 91
Eilers, A.-C., Hogg, D. W., Rix, H.-W., & Ness, M. K. 2019, ApJ, 871, 120
Ekström, S., Meynet, G., Chiappini, C., Hirschi, R., & Maeder, A. 2008, A&A, 489, 685
El Eid, M. F., Meyer, B. S., & The, L. S. 2004, ApJ, 611, 452
Evans, D. W., Riello, M., De Angeli, F., et al. 2018, A&A, 616, A4
Ezzeddine, R., Frebel, A., Roederer, I. U., et al. 2019, ApJ, 876, 97
Fabricius, C., Luri, X., Arenou, F., et al. 2021, A&A, 649, A5
Farah, A. M., Edelman, B., Zevin, M., et al. 2023, ApJ, 955, 107
Farmer, R., Laplace, E., de Mink, S. E., & Justham, S. 2021, ApJ, 923, 214
Farmer, R., Laplace, E., Ma, J.-z., de Mink, S. E., & Justham, S. 2023, ApJ, 948, 111
Farmer, R., Renzo, M., de Mink, S. E., Marchant, P., & Justham, S. 2019, ApJ, 887, 53
Farouqi, K., Kratz, K.-L., Pfeiffer, B., et al. 2010, ApJ, 712, 1359
Feroz, F., & Hobson, M. P. 2008, MNRAS, 384, 449
Feroz, F., Hobson, M. P., & Bridges, M. 2009, MNRAS, 398, 1601
Feroz, F., Hobson, M. P., Cameron, E., & Pettitt, A. N. 2019, OJAp, 2, 10
Fields, C. E., & Couch, S. M. 2020, ApJ, 901, 33
Fink, M., Kromer, M., Seitenzahl, I. R., et al. 2014, MNRAS, 438, 1762
Foley, R. J., Brown, P. J., Rest, A., et al. 2010, ApJL, 708, L61
Foreman-Mackey, D., Hogg, D. W., Lang, D., & Goodman, J. 2013, PASP, 125, 306
Fraser, M., Casey, A. R., Gilmore, G., Heger, A., & Chan, C. 2017, MNRAS, 468, 418
Frebel, A., Aoki, W., Christlieb, N., et al. 2005, Natur, 434, 871
Frebel, A., Christlieb, N., Norris, J. E., Aoki, W., & Asplund, M. 2006, ApJL, 638, L17
Frebel, A., & Norris, J. E. 2015, ARA&A, 53, 631
Frischknecht, U., Hirschi, R., Pignatari, M., et al. 2016, MNRAS, 456, 1803
Fröhlich, C., Martínez-Pinedo, G., Liebendörfer, M., et al. 2006, PhRvL, 96, 142502
Fujibayashi, S., Yoshida, T., & Sekiguchi, Y. 2015, ApJ, 810, 115
Fukugita, M., Ichikawa, T., Gunn, J. E., et al. 1996, AJ, 111, 1748
Gaia Collaboration, Brown, A. G. A., Vallenari, A., et al. 2018, A&A, 616, A1
Gaia Collaboration, Brown, A. G. A., Vallenari, A., et al. 2021, A&A, 649, A1
Gaia Collaboration, Prusti, T., de Bruijne, J. H. J., et al. 2016, A&A, 595, A1
Gallagher, A. J., Bergemann, M., Collet, R., et al. 2020, A&A, 634, A55
Gal-Yam, A. 2019, ARA&A, 57, 305
Gerber, J. M., Magg, E., Plez, B., et al. 2023, A&A, 669, A43
Green, G. M., Schlafly, E., Zucker, C., Speagle, J. S., & Finkbeiner, D. 2019, ApJ, 887, 93
Green, G. M., Schlafly, E. F., Finkbeiner, D. P., et al. 2014, ApJ, 783, 114
Grimmett, J. J., Heger, A., Karakas, A. I., & Müller, B. 2018, MNRAS, 479, 495
Grimmett, J. J., Müller, B., Heger, A., Banerjee, P., & Obergaulinger, M. 2021, MNRAS, 501, 2764
Gunn, J. E., Carr, M., Rockosi, C., et al. 1998, AJ, 116, 3040
Gunn, J. E., Siegmund, W. A., Mannery, E. J., et al. 2006, AJ, 131, 2332
Gustafsson, B., Edvardsson, B., Eriksson, K., et al. 2008, A&A, 486, 951
Hampel, M., Stancliffe, R. J., Lugaro, M., & Meyer, B. S. 2016, ApJ, 831, 171
Hartwig, T., Bromm, V., & Loeb, A. 2018, MNRAS, 479, 2202
Heger, A., Fryer, C. L., Woosley, S. E., Langer, N., & Hartmann, D. H. 2003, ApJ, 591, 288
Heger, A., & Woosley, S. E. 2002, ApJ, 567, 532
Heger, A., & Woosley, S. E. 2010, ApJ, 724, 341
Heiter, U., Lind, K., Bergemann, M., et al. 2021, A&A, 645, A106
Helmi, A., Babusiaux, C., Koppelman, H. H., et al. 2018, Natur, 563, 85
Herwig, F., Pignatari, M., Woodward, P. R., et al. 2011, ApJ, 727, 89
Herwig, F., Woodward, P. R., Lin, P.-H., Knox, M., & Fryer, C. 2014, ApJL, 792, L3
Holmbeck, E. M., Frebel, A., McLaughlin, G. C., et al. 2019, ApJ, 881, 5
Holmbeck, E. M., Sprouse, T. M., & Mumpower, M. R. 2023, EPJA, 59, 28
Hon, M., Huber, D., Kuszlewicz, J. S., et al. 2021, ApJ, 919, 131
Honda, S., Aoki, W., Ishimaru, Y., & Wanajo, S. 2007, ApJ, 666, 1189
Horta, D., Schiavon, R. P., Mackereth, J. T., et al. 2023, MNRAS, 520, 5671
Hunter, J. D. 2007, CSE, 9, 90
Husser, T. O., Wende-von Berg, S., Dreizler, S., et al. 2013, A&A, 553, A6
Imbriani, G., Limongi, M., Gialanella, L., et al. 2001, ApJ, 558, 903
Ishigaki, M. N., Tominaga, N., Kobayashi, C., & Nomoto, K. 2018, ApJ, 857, 46
Jeena, S. K., Banerjee, P., Chiaki, G., & Heger, A. 2023, MNRAS, 526, 4467
Jermyn, A. S., Bauer, E. B., Schwab, J., et al. 2023, ApJS, 265, 15
Ji, A. P., Li, T. S., Hansen, T. T., et al. 2020a, AJ, 160, 181
Ji, A. P., Li, T. S., Simon, J. D., et al. 2020b, ApJ, 889, 27
Ji, A. P., Simon, J. D., Frebel, A., Venn, K. A., & Hansen, T. T. 2019, ApJ, 870, 83
Ji, A. P., Simon, J. D., Roederer, I. U., et al. 2023, AJ, 165, 100
Johnson, J. A., & Bolte, M. 2002, ApJ, 579, 616
Jones, E., Oliphant, T., Peterson, P., et al. 2001, SciPy: Open source scientific tools for Python, http://www.scipy.org/
Karlsson, T., Johnson, J. L., & Bromm, V. 2008, ApJ, 679, 6
Kelson, D. D. 2003, PASP, 115, 688
Klessen, R. S., & Glover, S. C. O. 2023, ARA&A, 61, 65
Kolborg, A. N., Martizzi, D., Ramirez-Ruiz, E., et al. 2022, ApJL, 936, L26
Kollmeier, J. A., Zasowski, G., Rix, H.-W., et al. 2017, arXiv:1711.03234
Korotin, S. A., Andrievsky, S. M., & Zhukova, A. V. 2018, MNRAS, 480, 965
Kozyreva, A., Blinnikov, S., Langer, N., & Yoon, S. C. 2014, A&A, 565, A70
Kupka, F., Piskunov, N., Ryabchikova, T. A., Stempels, H. C., & Weiss, W. W. 1999, A&AS, 138, 119
Larsen, S. S., Eitner, P., Magg, E., et al. 2022, A&A, 660, A88
Li, H., Aoki, W., Matsuno, T., et al. 2022, ApJ, 931, 147
Li, H., Tan, K., & Zhao, G. 2018, ApJS, 238, 16
Limongi, M., & Chieffi, A. 2012, ApJS, 199, 38
Limongi, M., & Chieffi, A. 2018, ApJS, 237, 13
Lindegren, L., Bastian, U., Biermann, M., et al. 2021a, A&A, 649, A4
Lindegren, L., Klioner, S. A., Hernández, J., et al. 2021b, A&A, 649, A2
LSST Science Collaboration, Abell, P. A., Allison, J., et al. 2009, arXiv:0912.0201
Lugaro, M., Karakas, A. I., Stancliffe, R. J., & Rijs, C. 2012, ApJ, 747, 2
Macias, P., & Ramirez-Ruiz, E. 2018, ApJ, 860, 89
Magg, E., Bergemann, M., Serenelli, A., et al. 2022a, A&A, 661, A140
Magg, M., Schauer, A. T. P., Klessen, R. S., et al. 2022b, ApJ, 929, 119
Magg, M., Nordlander, T., Glover, S. C. O., et al. 2020, MNRAS, 498, 3703
Mainzer, A., Bauer, J., Cutri, R. M., et al. 2014, ApJ, 792, 30
Marocco, F., Eisenhardt, P. R. M., Fowler, J. W., et al. 2021, ApJS, 253, 8
Mashonkina, L., Sitnova, T., & Belyaev, A. K. 2017, A&A, 605, A53
McWilliam, A., Wallerstein, G., & Mottini, M. 2013, ApJ, 778, 149
Mckinney, W. 2010, in Proc. of the 9th Python in Science Conf., Data Structures for Statistical Computing in Python, ed. S. van der Walt & J. Millman (Austin, TX: SciPy), 56
Meynet, G., Ekström, S., & Maeder, A. 2006, A&A, 447, 623
Moriya, T., Tominaga, N., Tanaka, M., Maeda, K., & Nomoto, K. 2010, ApJL, 717, L83
Morton, T. D., 2015 isochrones: Stellar model grid package, Astrophysics Source Code Library, ascl:1503.010
Naidu, R. P., Conroy, C., Bonaca, A., et al. 2021, ApJ, 923, 92
Nicholl, M. 2021, A&G, 62, 5.34
Nishimura, N., Sawai, H., Takiwaki, T., Yamada, S., & Thielemann, F. K. 2017, ApJL, 836, L21
Nomoto, K., Kobayashi, C., & Tominaga, N. 2013, ARA&A, 51, 457
Nordlander, T., & Lind, K. 2017, A&A, 607, A75
Norris, J. E., Yong, D., Bessell, M. S., et al. 2013, ApJ, 762, 28
Offner, S. S. R., Clark, P. C., Hennebelle, P., et al. 2014, in Protostars and Planets VI, ed. H. Beuther et al. (Tucson, AZ: Univ. of Arizona Press), 53
Onken, C. A., Wolf, C., Bessell, M. S., et al. 2019, PASA, 36, e033
Orkney, M. D. A., Laporte, C. F. P., Grand, R. J. J., et al. 2023, MNRAS, 525, 683
Paxton, B., Bildsten, L., Dotter, A., et al. 2011, ApJS, 192, 3
Paxton, B., Cantiello, M., Arras, P., et al. 2013, ApJS, 208, 4
Paxton, B., Schwab, J., Bauer, E. B., et al. 2018, ApJS, 234, 34
Paxton, B., Smolec, R., Schwab, J., et al. 2019, ApJS, 243, 10
Pejcha, O., & Thompson, T. A. 2015, ApJ, 801, 90
Penoyre, Z., Belokurov, V., Wyn Evans, N., Everall, A., & Koposov, S. E. 2020, MNRAS, 495, 321
Perego, A., Hempel, M., Fröhlich, C., et al. 2015, ApJ, 806, 275
Pignatari, M., Gallino, R., Meynet, G., et al. 2008, ApJL, 687, L95
Placco, V. M., Frebel, A., Beers, T. C., & Stancliffe, R. J. 2014, ApJ, 797, 21
Placco, V. M., Frebel, A., Beers, T. C., et al. 2016, ApJ, 833, 21
Placco, V. M., Frebel, A., Lee, Y. S., et al. 2015, ApJ, 809, 136
Placco, V. M., Sneden, C., Roederer, I. U., et al., 2021, linemake: Line list generator, Astrophysics Source Code Library, ascl:2104.027
Plez, B., 2012, Turbospectrum: Code for spectral synthesis, Astrophysics Source Code Library, ascl:1205.004

Price-Whelan, A., Sipőcz, B., Wagg, T., et al. 2022, adrn/gala: v1.6.1, Zenodo, doi:10.5281/zenodo.7299506
Price-Whelan, A. M. 2017, JOSS, 2, 388
Price-Whelan, A. M., Sipőcz, B. M., Günther, H. M., et al. 2018, AJ, 156, 123
Pruet, J., Hoffman, R. D., Woosley, S. E., Janka, H. T., & Buras, R. 2006, ApJ, 644, 1028
Pruet, J., Thompson, T. A., & Hoffman, R. D. 2004, ApJ, 606, 1006
R Core Team, 2023, R: A Language and Environment for Statistical Computing, v4.3.2, https://www.R-project.org/
Reggiani, H., Amarsi, A. M., Lind, K., et al. 2019, A&A, 627, A177
Reggiani, H., Schlaufman, K. C., & Casey, A. R. 2023, AJ, 166, 128
Riello, M., De Angeli, F., Evans, D. W., et al. 2018, A&A, 616, A3
Ritter, C., Herwig, F., Jones, S., et al. 2018, MNRAS, 480, 538
Roederer, I. U., & Barklem, P. S. 2018, ApJ, 857, 2
Roederer, I. U., Karakas, A. I., Pignatari, M., & Herwig, F. 2016, ApJ, 821, 37
Roederer, I. U., Lawler, J. E., Den Hartog, E. A., et al. 2022, ApJS, 260, 27
Roederer, I. U., Sakari, C. M., Placco, V. M., et al. 2018, ApJ, 865, 129
Rowell, N., Davidson, M., Lindegren, L., et al. 2021, A&A, 649, A11
Ryan, S. G., Norris, J. E., & Beers, T. C. 1996, ApJ, 471, 254
Skúladóttir, Á., Salvadori, S., Amarsi, A. M., et al. 2021, ApJL, 915, L30
Salvadori, S., Bonifacio, P., Caffau, E., et al. 2019, MNRAS, 487, 4261
Sana, H., de Mink, S. E., de Koter, A., et al. 2012, Sci, 337, 444
Schauer, A. T. P., Drory, N., & Bromm, V. 2020, ApJ, 904, 145
Schlaufman, K. C., & Casey, A. R. 2014, ApJ, 797, 13
Schlegel, D. J., Finkbeiner, D. P., & Davis, M. 1998, ApJ, 500, 525
Semenova, E., Bergemann, M., Deal, M., et al. 2020, A&A, 643, A164
Sharda, P., & Krumholz, M. R. 2022, MNRAS, 509, 1959
Siegel, D. M., Barnes, J., & Metzger, B. D. 2019, Natur, 569, 241
Sieverding, A., Kresse, D., & Janka, H.-T. 2023, ApJL, 957, L25
Skrutskie, M. F., Cutri, R. M., Stiening, R., et al. 2006, AJ, 131, 1163
Smee, S. A., Gunn, J. E., Uomoto, A., et al. 2013, AJ, 146, 32
Sneden, C. A. 1973, PhD thesis, The Univ. of Texas at Austin
Sobeck, J. S., Kraft, R. P., Sneden, C., et al. 2011, AJ, 141, 175
Speagle, J. S. 2020, MNRAS, 493, 3132
Starkenburg, E., Martin, N., Youakim, K., et al. 2017, MNRAS, 471, 2587
Stassun, K. G., Collins, K. A., & Gaudi, B. S. 2017, AJ, 153, 136
Stassun, K. G., Corsaro, E., Pepper, J. A., & Gaudi, B. S. 2018, AJ, 155, 22
Stassun, K. G., & Torres, G. 2016, AJ, 152, 180
Stassun, K. G., & Torres, G. 2021, ApJL, 907, L33
Storm, N., & Bergemann, M. 2023, MNRAS, 525, 3718
Suda, T., Katsuta, Y., Yamada, S., et al. 2008, PASJ, 60, 1159
Sukhbold, T., Ertl, T., Woosley, S. E., Brown, J. M., & Janka, H. T. 2016, ApJ, 821, 38
Surman, R., McLaughlin, G. C., & Hix, W. R. 2006, ApJ, 643, 1057
Takahashi, K., Yoshida, T., & Umeda, H. 2018, ApJ, 857, 111
Tayar, J., & Joyce, M. 2022, ApJL, 935, L30
Tominaga, N. 2009, ApJ, 690, 526
Torra, F., Castañeda, J., Fabricius, C., et al. 2021, A&A, 649, A10
Umeda, H., & Nomoto, K. 2002, ApJ, 565, 385
van der Walt, S., Colbert, S. C., & Varoquaux, G. 2011, CSE, 13, 22
Voronov, Y. V., Yakovleva, S. A., & Belyaev, A. K. 2022, ApJ, 926, 173
Wanajo, S. 2006, ApJ, 647, 1323
Wanajo, S. 2013, ApJL, 770, L22
Wanajo, S., Müller, B., Janka, H.-T., & Heger, A. 2018, ApJ, 852, 40
Waskom, M., Botvinnik, O., O'Kane, D., et al. 2016, seaborn: v0.7.0 (January 2016), Zenodo, doi:10.5281/zenodo.45133
Woodward, P. R., Herwig, F., & Lin, P.-H. 2015, ApJ, 798, 49
Woosley, S. E. 2017, ApJ, 836, 244
Woosley, S. E., & Hoffman, R. D. 1992, ApJ, 395, 202
Wright, E. L., Eisenhardt, P. R. M., Mainzer, A. K., et al. 2010, AJ, 140, 1868
Xing, Q.-F., Zhao, G., Liu, Z.-W., et al. 2023, Natur, 618, 712
Yakovleva, S. A., Belyaev, A. K., & Bergemann, M. 2020, Atoms, 8, 34
Yong, D., Kobayashi, C., Da Costa, G. S., et al. 2021, Natur, 595, 223
Yoon, S. C., Dierks, A., & Langer, N. 2012, A&A, 542, A113
York, D. G., Adelman, J., Anderson, John, E. J., et al. 2000, AJ, 120, 1579